2020-09-22

Impact of Water Saturation on Gas Storage in Clay-rich Shale

Zhu, Lihua

UNIVERSITY OF CALGARY

IMPACT OF WATER SATURATION ON GAS STORAGE IN CLAY-RICH SHALE

by

Lihua Zhu

A THESIS

SUBMITTED TO THE FACULTY OF GRADUATE STUDIES

IN PARTIAL FULFILMENT OF THE REQUIREMENTS FOR THE

DEGREE OF MASTER OF SCIENCE

GRADUATE PROGRAM IN CHEMICAL ENGINEERING

CALGARY, ALBERTA

SEPTEMBER, 2020

Abstract

For shale gas reservoirs, to evaluate the total gas-in place (GIP) requires us to estimate the adsorbed gas amount accurately because the adsorbed gas generally constitutes 40%-85% of the total GIPs. However, under geologic conditions, water saturations always exist in shale reservoirs, which largely decreases the natural gas adsorption capability of shale, thus affecting the reliability of shale gas resources evaluation. In this thesis, we have built a mathematical model for calculations about gas adsorption in shale clay in different water environments, where the Langmuir adsorption equation is adopted for the gas-liquid interaction between methane and dry clay surface, and the Gibbs equation is used to characterize the gas-liquid interaction between methane and an adsorbed water film. Through our calculation, with the water saturation in a 4-nm slit pore being 20%, methane adsorption capacity is decreased by 55.4%, compared with dry conditions; when the water saturation in a 4-nm capillary is 36%, methane adsorption capacity is decreased by 80%. This proposed model is then extended to porous media which follows the log-normal pore size distribution (PSD). Based on the results, we have found that the shapes and sizes of nanopores in shale can affect the moisture distribution features and gas adsorption capability. Influences of water on methane adsorption capability mainly acts as (i) an adsorbed water film in large pores decreases the affinity between methane and pore-walls; (ii) capillary water totally blocks some small pores and makes them loose abilities to adsorb methane. When the water saturation of the slit-pore porous media reaches 43%, with the 2-nm slit pores blocked by water, the gas adsorption capability declines by 50% compared with dry conditions. When the water saturation of the capillary porous media arrives at 45%, with the 3-nm slit pores blocked by moisture, the methane adsorption capacity is deceased by 70% compared with dry conditions.

Dedication

To my mother,

for her care, patience, and love

in all stages of my life.

Acknowledgements

My deepest appreciation goes to my supervisor, Dr. Zhangxing (John) Chen, for his generous support and encouragement throughout my journey at the University of Calgary. Especially during my hardest time in the COVID-19 pandemic, his patience and kind concern gave me more faith and led me to gradually go beyond my mental fragility. I also want to thank my committee members, Dr. Jinguang Hu and Dr. Uttandaraman Sundararaj, for their precious comments on my thesis.

My appreciation also extends to the Reservoir Simulation Group. In particular, I want to acknowledge Dr. Jing Li for assisting me to find my research interest and dive into the research area. Without his professional assistance and valuable suggestions, I would still have a lot of detours to make. Additionally, I want to thank our group member Mr. Renjie Yu, for his precious advice on data selections in my model verification process, and Mr. Stephen Cartwright for the timely software support. My friend Ms. Lei Wang is also acknowledged for viewing my entire thesis and helping with the format.

To my mom: As the best mother in the world, and the best person I know who holds the strongest will power and good qualities, my mother deserves my most sincere appreciation for showing me the power of unconditional love and guiding me towards the true values of life. She is the reason that I get up in the morning and will continue to be my lifelong inspiration. “For you, a thousand times over.”

Table of contents

List of Tables

List of Figures

List of Symbols, Abbreviations and Nomenclature

Symbol	Definition
A	Specific surface area of clay, m^2/g
A_{eff}	Effective specific surface area for methane adsorption in a capillary, m^2/g
A_f	Surface area of the aqueous film, m^2
$A_{capillary}$	Specific surface area of a capillary, m^2/g
A_{slit}	Specific surface area of one crystal layer of clay in a slit pore, m^2/g
A_{H20}	Area of the clay surface covered by water molecules, m^2
A_{total}	Total surface area of clay, m2
A_H	Hamaker constant for the clay-water-gas interaction, J
D^*	Average pore diameter, nm
D	Capillary diameter, nm
H	Interlayer spacing, nm
H^*	Effective width of the slit pore, nm
h	Water film thickness, nm
k	Coefficient for structural force, N/m^2
K	The maximum amount of adsorbed gas per surface area (gas-solid), mmol/g;
M_{CH4}	Mole mass of methane, 16g/mol
$n_{max\text{-}dry}$	The maximum amount of adsorbed gas in dry clay, mmol/g
$n_{ad\text{-}dry}$	Amount of adsorbed gas in dry clay, mmol/g
$n_{ad\text{-}wet}$	Methane adsorption amount on the surface of the aqueous film, mmol/g

$n_{ad\text{-}mix}$	Amount of adsorbed gas on the dry clay and on the surface of the aqueous film, mmol/g
$n_{bulk\text{-}slit}$	Molar amount of free gas inside slit pores, mmol/g
$n_{T\text{-}slit}$	Total adsorbed and free gas inside slit pores, mmol/g
$n_{ad}(i)$	Methane adsorption amount in a single slit pore or capillary, mmol/g
$n_{ad\text{-}T}$	Total adsorption in porous media, mmol/g
r	Capillary radius, nm
R	Gas constant, 8.314 J/(mol·K)
RH	Relative humidity
S_{mon}	Water saturation in the pore with exactly monolayer moisture coverage
$S_w(i)$	Water saturation in a single pore
S_w	Water saturation of a porous media
T	Temperature of the reservoir, K
P_c	Capillary pressure, MPa
P_c^*	Cylindrical capillary pressure in a capillary, MPa
P_0	Saturated vapor pressure of pure water, MPa
P_0^*	Saturated vapor pressure of the liquid film, MPa
P_g	Gaseous phase pressure, MPa
P_f	Water film pressure, MPa
P_L	Langmuir pressure (gas-solid), MPa
P^*	Langmuir pressure (gas-liquid), MPa
P_v	Partial pressure of water vapor, MPa;
P_w	Bulk water pressure, MPa
V_T	Total pore volume of porous media
V_{wT}	Total water volume inside single pores of different sizes
x_A	Mole fraction of pure water in the water film

Z	Free gas compression factor
γ	Methane-water surface tension, mN/m
$\Pi(h)$	Disjoining pressure, MPa
Π_m	Intermolecular force, MPa
Π_{el}	Electrostatic force, MPa
Π_{st}	Structural force, MPa
α	Water coverage coefficient
ε	Relative dielectric constant
ε_0	Vacuum dielectric constant, F/m
ζ_1	Electric potential of the clay surface, mV
ζ_2	Electric potential of the clay surface, mV
λ	Characteristic length of water molecules, nm.
Γ	Adsorbed gas amount per surface area (gas-liquid), mmol/m^2
Γ^*	The maximum adsorbed gas amount per surface area (gas-liquid), mmol/m^2
Δ	Distance from oxygen atoms in clay to oxygen atoms in water molecules, nm
$\Delta\mu_1$	Adsorption potential for per molar water vapor, J
$\Delta\mu_2$	Work (or energy change) caused by disjoining pressure
$\bar{\rho}_{CH_4}$	Average density of methane, g/cm^3
ρ^*_{H2O}	Density of liquid water, 1g/mol
ϕ_i	Pore volume fraction
σ	Standard deviation of a log-normal distribution
u	Logarithmic mean of a log-normal distribution

Abbreviations

DLOV	Derjaguin-Landau-Verwey-Overbeek Theory (Water film theory)
CBW	Clay bound water

TRR	Total technically recoverable resources
PSD	Pore size distribution
VOC	Volatile organic compounds

Chapter 1 Introduction

1.1 Overview of Shale Gas Resource

Since the 21st century, shale gas has attracted much attention as an essential unconventional gas resource, becoming a hotspot of recent energy research. Among the overall worldwide recoverable reserves of unconventional gas, shale gas encompasses 71.1% (Hongjun et al., 2016), as shown in Figure 1-1.

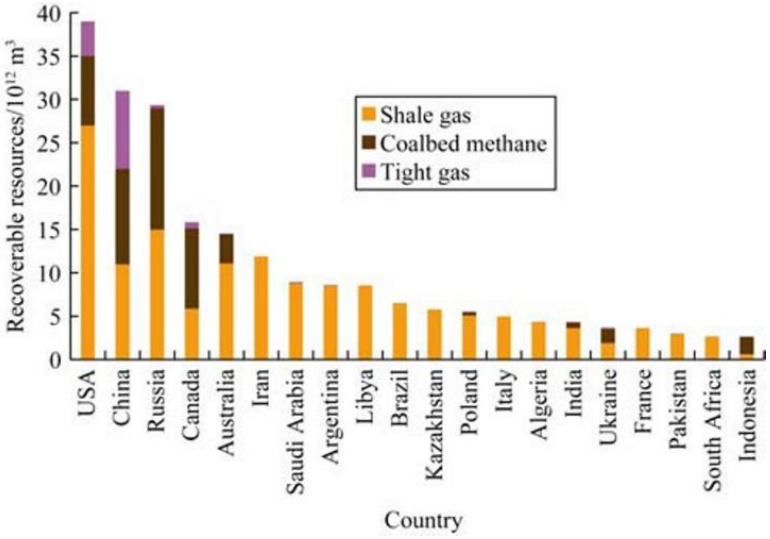

Figure 1-1 Unconventional gas resources by countries (Hongjun et al., 2016)

The total technically recoverable resources (TRRs) of shale gas worldwide are estimated at 7576.6 trillion cubic feet by EIA (EIA, 2015), including both economic and uneconomic resources, found in 137 basins located in 41 countries. As shown in Figure 1-2, shale gas is scattered all over the world, with 862 trillion cubic feet in the US and 1,275 trillion cubic feet in China (Zhiltsov et al., 2016). In the United States, shale gas occupies 68% of the total gas reserves (EIA, 2019).

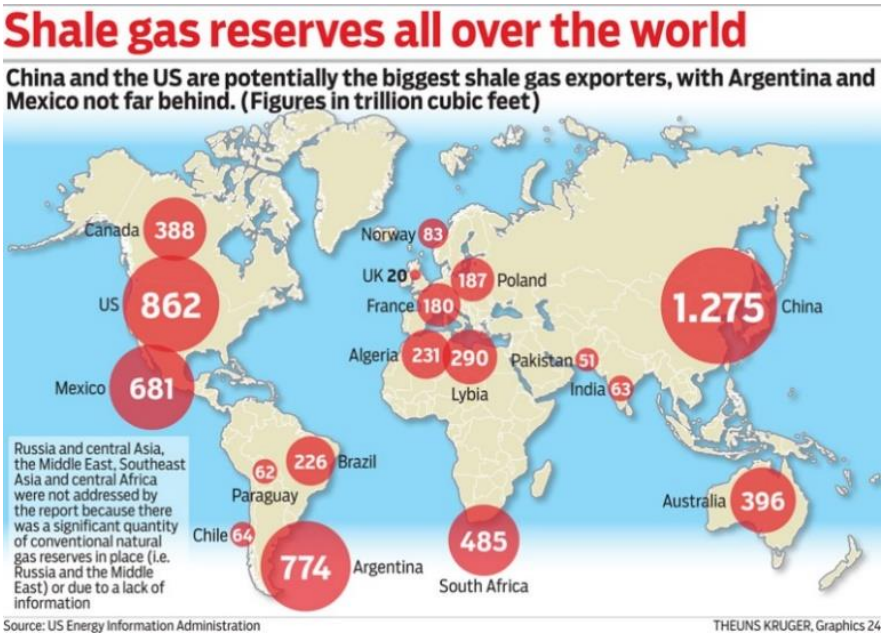

Figure 1-2 Global distributions of shale gas resources (Zhiltsov et al., 2016)

A pore-fracture system of shale rock is where most shale gas is located. Within this pore-fracture system, the gas exists in a free state, an adsorbed state and a small amount of dissolved state. It has features of self-storage, self-generation, low porosity, and low permeability (Yang et al., 2020). Under original conditions, shale reservoirs generally have a certain water saturation. Based on logging data, the water saturation in typical shale gas blocks in U.S. and China is given by Table 1.1. The moisture significantly influences shale's gas adsorption capability, which causes difficulties in resource evaluation and accurate prediction of a reservoir's productive capacity.

Table 1-1 Water saturation of main shale strata in America

Main Shale Strata in North America and China	Water Saturation
Barnett	25%~35%
Haynesville	15%~35%
Eagle Ford	<20%
Marcellus	12%~35%
Fayetteville	25%~50%
ChangLing—WeiYuan	40%~46%
Fushun—YongChuang	33%~39%

1.2 Overview of Water/gas Distribution in Gas Shale

1.2.1 Water/gas Distribution in Organic Pores

Under reservoir conditions, the existence of moisture in organic pores is still controversial. The surface properties (wettability), pore size, and morphological characteristics of organic pores are the main factors that determine whether water can enter organic pores (Passey et al., 2010). Based on recent research, it has been proven that the water content in kerogen pores may be controlled by a kerogen type, maturity (degree of thermal evolution), and functional groups (Hu, 2016; Sang et al., 2019; Sui et al., 2020).

Hu (2014) simulated distributions of hydrocarbon molecules and water molecules in kerogen pores. As indicated by the simulation, functional groups on a pore surface causes hydrophilicity of organic pores. As shown in Figure 1-3, for kerogen pores containing polar functional groups, water molecules tend to form water clusters near the functional groups and coexist with hydrocarbon molecules in the pores. But for kerogen pores without functional groups,

water molecules cannot enter into the pores, and the pores are instead filled by hydrocarbon molecules.

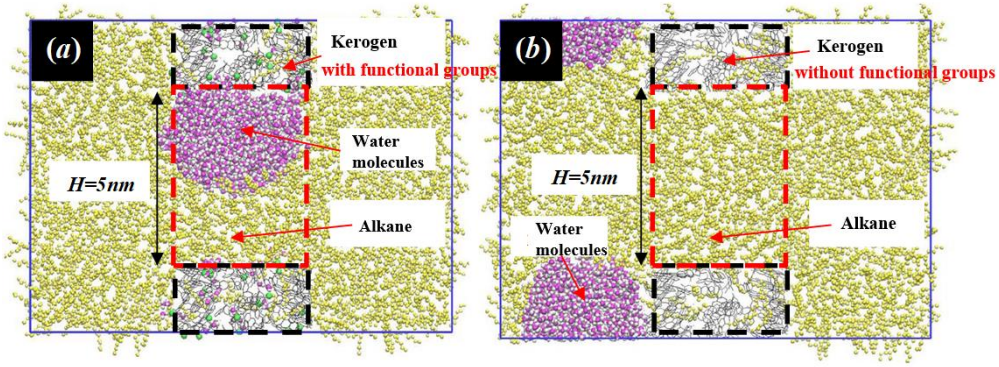

Figure 1-3 Hydrocarbon-water distribution characteristics inside kerogen pores (a) with functional groups and (b) without functional groups (Hu, 2014)

Furthermore, Hu (2015) studied the distribution characteristics of a fracturing fluid in kerogen pores with different sizes through molecular simulations, and the results showed that a pore size also affects the accessibility of liquid water to organic pores. The hydrophobic force of organic matter will prevent liquid water (fracturing fluid) from entering pores smaller than 0.9 nm; however, the fracturing fluid is able to enter the pores which are larger than 1.2 nm, as shown in Figure 1-4.

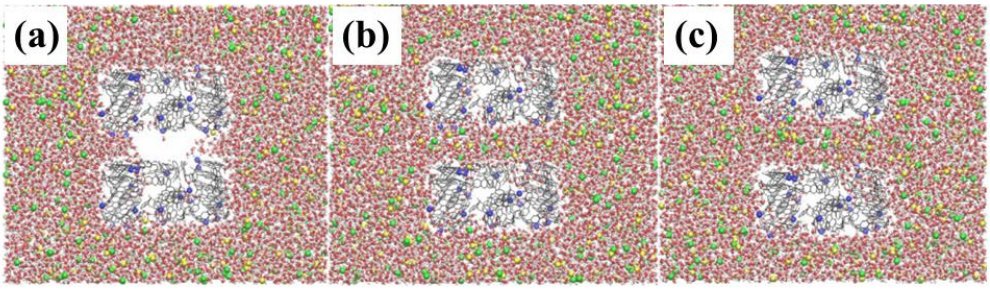

Figure 1-4 Distribution of fracturing fluid inside (a) 0.9-nm kerogen pore (b) 1.2-nm kerogen pore (c) 1.6-nm kerogen pore (Hu, 2015)

1.2.2 Water/gas Distribution in Inorganic Pores

Compared with the water distribution characteristics of organic pores, scholars have a unified understanding of the water distribution characteristics of inorganic pores. Since the inorganic minerals are strongly hydrophilic, a water film with a thickness of about 0.3 to 0.4 nm always adsorbs on a pore surface (Passey et al., 2010), as shown in Figure 1-5. Especially for clay minerals, water molecules and clay particles can be tightly combined through electrostatic forces.

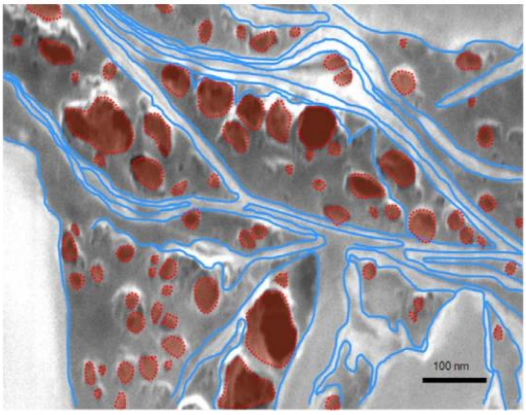

Figure 1-5 Water film on clay surface (Parsey et al., 2010)

For natural shale samples, the clay bound water (CBW) of shale clay accounts for a non-negligible proportion of the bulk volume of clay, at around 2.63% to 7.19% measured by Tight Rock Analysis (TRA) technology (Korb et al., 2014). This moisture content has affected the measurement of shale porosity, as shown in Figure 1-6. In addition, because water molecules and clay surfaces have a strong electrostatic interaction, the clay-bound water is difficult to remove, and thus the bound water always exists under reservoir conditions.

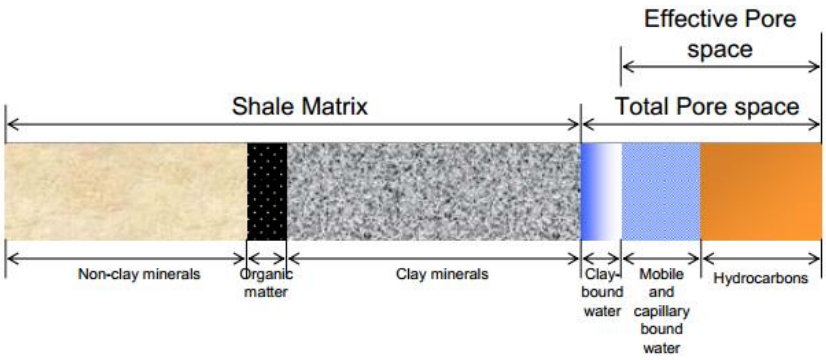

Figure 1-6 Fluids distribution characteristics inside gas-shale pore system (Passey et al., 2010)

Using molecular simulation methods, Jin and Firoozabadi (2013, 2014) studied the adsorption of methane and moisture inside 4-nm montmorillonite pores. Their results showed that if the water saturation in pores is low, water films are adsorbed on pore surfaces while methane molecules are mostly located in pore centers as free gas and. With a high moisture content, the pores are almost filled by water molecules, and methane molecules can only dissolve in the pore water but cannot adsorb on a pore surface (Figure 1-7).

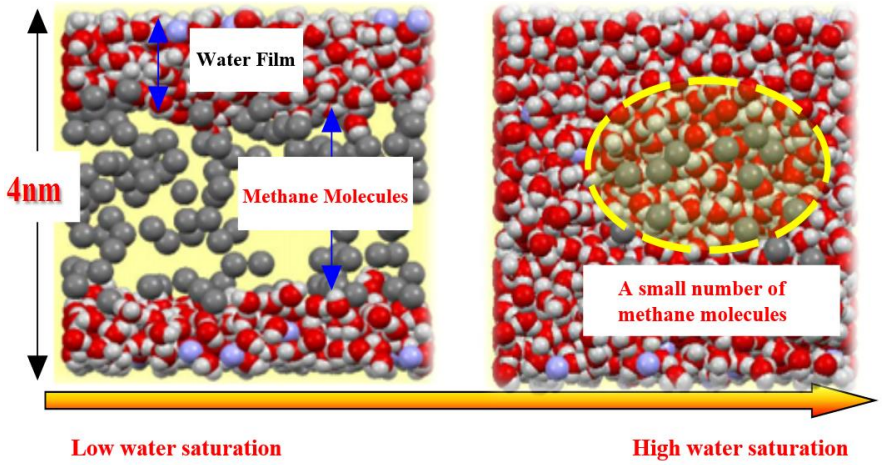

Figure 1-7 Gas-water distribution characteristics inside clay pores (a) with low water saturation and (b) with high water saturation (Jin and Firoozabadi, 2014)

1.3 Overview of Gas/water Adsorption Mechanism in Gas Shale

1.3.1 Gas/water Adsorption in Organic Pores (Shale Kerogen)

The influence of moisture in the gas adsorption capability in shale kerogen largely depends on hydrophobic and hydrophilic adsorption sites distributed in an entire kerogen pore network (Chalmers and Bustin, 2010). For kerogen pores with low maturity (Figure 1-8, a), moisture is able to be adsorbed on some aliphatic organic matters because there are many polar adsorption sites. As maturity increases, organic matter surfaces change from aliphatic to aromatic and the polar adsorption sites decrease; as a result, the hydrophilicity of the kerogen pores weakens (Figure 1-8, b) and the methane adsorption capacity increases. For hydrophilic pores, pore throats may be blocked by water molecules, preventing methane molecules from entering the pores (Figure 1-8, c).

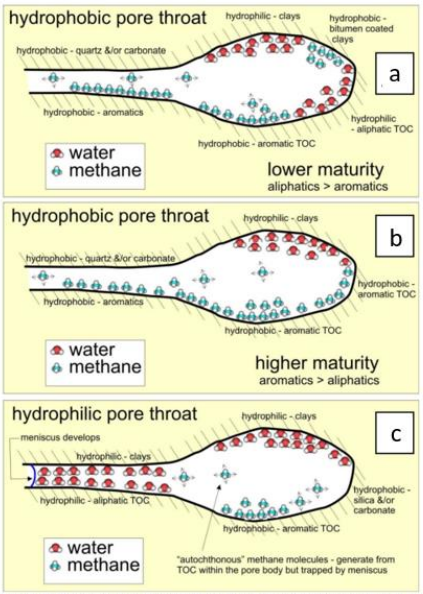

Figure 17: Schematic pore model for the hydrophilic and hydrophobic sorption sites within an organic rich gas shale. Although methane is generated in local pores, if pore throats are hydrophilic, water may block pore networks that allow gas to flow through the matrix of the reservoir. As shown in Figure 11 there is a lag between the removal of water from a meniscus and the decrease in pressure (hysteresis effect).

Figure 1-8 Gas-water distribution characteristics inside kerogen pores with different wettability (Chalmers and Bustin, 2010)

1.3.2 Gas/water Adsorption in Inorganic Pores (Shale Clay)

For clay-rich gas shale, the natural gas adsorption in inorganic pores, especially clay pores, are also non-negligible. Since clay minerals also have tiny pores of less than 10 nm, shale's gas adsorption ability is also controlled by clay minerals (Li et al, 2019).

Experiments showed that the saturated methane adsorption capacity for dry illite and kaolinite is 1.7~2.7 cm^3/g; montmorillonite is 8 cm^3/g; and clay-rich shale is 0.5~4 cm^3/g (Ji et al, 2014; Gu et al., 2018; Ross and Bustin, 2008, 2009). But under equilibrium moisture conditions, the abilities of shale and pure clay to adsorb methane are greatly reduced (Luo et al., 2019).

The natural gas adsorption capacities of shale and clay under moist and dry conditions are given in Figure 1-9. Under equilibrium water conditions, the gas adsorption amount of pure clay declines by as much as 70% to 90%. Indeed, while the amount of gas adsorbed in shale declines by 20% to 90%, the reduction rate mainly depends on the content of clay minerals.

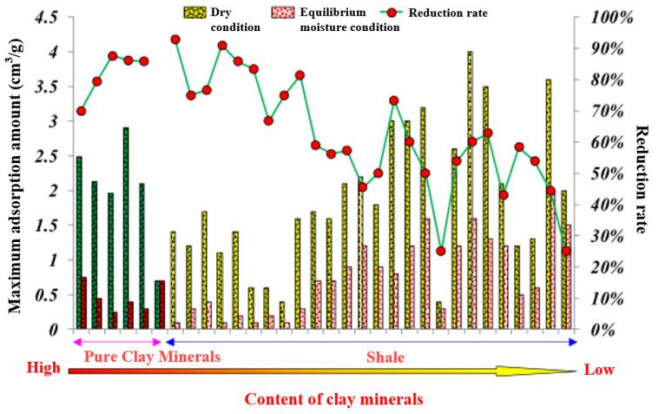

Figure 1-9 Methane adsorption capacities in clay and shale under moist and dry conditions (Ross and Bustin, 2008, 2009; Gasparik, 2012)

Similarly, Merkel et al. (2016) showed that compared with clay minerals, the impact of water on kerogen's capability to adsorb methane is negligible. Therefore, the influence of water

on shale's capability to adsorb natural gas is mainly dictated by the inorganic minerals content, such as shale clay.

Taking the adsorption rates of organic gas and water on soil (Ho and Webb, 2006) as a reference, we can further study the adsorptions of methane and water on shale as shown in Figure 1-10. With the environment having a low humidity, the moisture content of the soil is low, and a particle surface only adsorbs scattered water molecules (Figure 1-10, a). In this case, organic gas mainly exists as: (i) directly adsorbed on a soil surface, such as the organic matter in the soil (gas-solid interface adsorption); (ii) partly adsorbed on a surface of water molecules (gas-liquid interface adsorption); or (iii) competitively adsorbed with water molecules in micropores (micropore filling). When the relative humidity of an environment is high, however, continuous water films bond on a surface of soil particles (Figure 1-10, b). In this case, organic gas mainly exists as: (iv) adsorbed on a surface of a water film (gas-liquid interface adsorption); (v) dissolved in the water film; or (vi) adsorbing of the dissolved gas on a soil surface (liquid-solid interface adsorption).

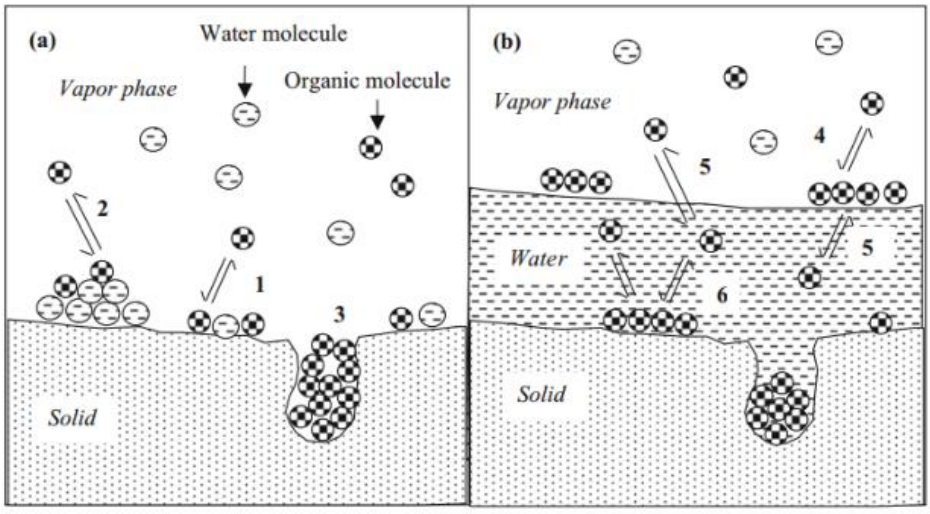

Figure 1-10 Distribution characteristics of organic gas and water molecules in soil

1.4 Problems

Based on the overview, there are two main problems found in the present research:

(i) The current evaluation of gas-water distributions in shale reservoirs is too macroscopic, and it does not reflect the difference of the gas-water distributions in different sizes and types of pores (organic-inorganic pores) in shale.

Including both inorganic and organic matters, shale has a complex composition. Due to the different wettability of inorganic and organic matters, the water contents in inorganic and organic pores are completely dissimilar. In organic pores, the water content may be determined by factors like functional group content and maturity of kerogen; for inorganic pores, the water content cannot be ignored.

However, the current research generally uses logging curves to evaluate the initial water saturation in a whole reservoir, without considering the moisture distribution features at the micro level. In particular, there has been a lack of quantitative research on the thickness of the thin wetting film in differently sized inorganic pores.

(ii) At present, the Langmuir model has been adopted by most researches, which outlines gas-solid interface adsorption. However, actual shale reservoirs generally contain water saturation, and thus the Langmuir model cannot describe the complex gas-liquid-solid interactions present within many such reservoirs.

Considering the differences in water distributions found in inorganic and organic pores, the mechanisms of methane adsorption in these pores are completely different. For non-polar organic pores, a high maturity often corresponds to a relatively low water content and methane is mainly adsorbed on pore surfaces, thus constituting gas-solid interface adsorption. Yet, if the maturity is

low, the water content is relatively high within the pores, and methane and water act as competitive adsorption. In addition, for polar inorganic pores, if the pore water content is low, a water film first occupies a pore surface and thus methane is generally adsorbed on the liquid film, which encompasses gas-liquid adsorption. Indeed, with the pore having a high moisture content, the methane molecules can only be dissolved in water.

And yet, the Langmuir adsorption model has always been adopted by current researches to evaluate the capacities for natural gas adsorption of shale. While it well describes the gas-solid interface adsorption between methane and dry samples, in actual reservoirs with certain water saturations, the Langmuir model cannot accurately describe the complex gas-liquid-solid three-phase interactions found within these reservoirs.

1.5 Research Objectives

(i) In this work, we first study gas-water distribution characteristics in shale, and establish a mathematical model to calculate the thicknesses of water films in nano-scale clay pores.

(ii) Then, based on the gas-water distribution characteristics, we study both gas-liquid-solid interactions and gas storage characteristics present within shale gas reservoirs, and establish the corresponding mathematical models to calculate the methane adsorption capacity in nano-scale shale clay pores under given moisture conditions.

(iii) Finally, we extend these mathematical models from a single pore case to a porous shale case with a certain pore size distribution (PSD). The corresponding moisture distributions and its influence in gas storage features in porous shale have been analyzed.

1.6 Organization of the Thesis

Chapter 1 introduces shale gas resources, water/gas distribution features and water/gas adsorption mechanisms found in shale. Problems in the present research, thesis objectives and the organization of the thesis are also stated.

Chapter 2 introduces a gas storage space and characteristics in shale reservoirs and describes initial water saturations and distributions in inorganic and organic pores. The “ultra-low water saturation" concept is stated.

Chapter 3 illustrates a mathematical model of the aqueous film thickness inside nano-scale clay pores in shale, and performs both thermodynamic equilibrium analysis and mechanical equilibrium analysis of a clay-bound water film. The various thicknesses of the wetting films under various relative humidity are calculated and the effect of a pore shape (both slit pores and capillary) on the water film thickness is discussed.

Chapter 4 establishes a mathematical model for characterizing natural gas adsorption in shale clay pores under both dry and moist conditions. Methane adsorption isotherms under different water saturations are calculated, and impacts of moisture on gas adsorption capability are discussed. Model validation is conducted by comparing our calculated results to molecular simulation results.

Chapter 5 extends the methane adsorption model to a porous media case. The water saturations under various relative humidity are obtained in porous shale with a log-normal pore size distribution (PSD). Moisture distribution features of differently sized pores under various relative humidity are obtained. Finally, the methane adsorption isotherms in porous media under different water saturations are calculated.

Chapter 6 summarizes research results and indicates future study and potential improvements.

Chapter 2 Gas/water Storage Characteristics and Water Saturation in Shale

2.1 Gas storage characteristics and space in Shale

For gas in shale, there are three states of existence: (i) an adsorbed state, which mainly exists on surfaces of the matrix and organic particles; (ii) a free state, mainly existing in natural cracks, matrix and organic pores; and finally, (iii) a dissolved state. Because shale reservoirs have very low water content, generally less than 0.1%, the dissolved gas content is negligible and can often be ignored. From previous studies, the adsorbed gas content found in shale is generally greater than 40%. The content of shale gas far exceeds a pore volume of shale owing to the gas in an adsorbed state.

Based on their location and origin, pores and fractures in shale can be put into the following five categories:

(i) Clay mineral inter-granular pores

Clay minerals account for 16.8%-70.1% of shale composition and are fundamental mineral components of shale. Large quantities of inter-granular pores are found in clay minerals.

(ii) Rock skeleton mineral pores

The pores found in rock skeleton minerals are nano-scale pores formed by quartz and feldspar dissolution. In addition, there are mineral cleavage cracks, crystal gaps and intracrystalline pores. The pores of rock skeleton minerals are usually disconnected.

(iii) Paleontological fossil pores

Paleontological fossils exist in some shale rock samples, such as gastropod algae fossils and ostracod fossils. These microfossils vary in size from 12 to 800 μm in length, and they are relatively intact. Micropores can be found in the skeleton and cavity of paleontological microfossils, whose diameter can reach 30μm. The shape of paleontological fossil pores is related

to a microfossil structure, which can be ellipsoid, slit, polygonal and irregular. This type of pores has both a large scale and good connectivity, but it is relatively rare.

(iv) Organic pores

An abundance of nano-scale pores can be found inside organic particles in shale. These are known as organic pores or organic nanopores. The organic nanopores are mainly spherical or ellipsoidal, with the pore sizes ranging from 8 to 950 nm.

(v) Micro cracks

Experiments have found that organic matter, particle skeleton minerals, and clay minerals in shale can develop micro-cracks. The micro-cracks inside shale particles are generally quite straight, with less tortuosity and less cement filling, while the micro-cracks between particles are curved in a zigzag shape. The length of these micro-cracks ranges from 5.5-12μm, and the crack spacing can reach more than 50 nm.

2.2 Water Saturation in Organic and Inorganic Pores

Shale is a complex sedimentary rock with thin layered joints, which is mainly formed by clay and organic matter under sedimentation, and a mixture of quartz, feldspar and other brittle minerals. Generally, the mineral composition of shale rock includes 30% to 50% of clay minerals, 15% to 25% of brittle minerals, and 4% to 20% of organic matter (Rezaee, 2015).

Shale gas can fall into three categories according to a shale deposition environment: continental, marine, and marine-continental transitional shale gas. Marine shale gas is formed by shales found in saltwater sedimentary environments such as shallow sea ocean or marine basin. Terrestrial shale gas is formed by shales found in freshwater sedimentary environments such as continental rivers, lakes and swamps. A static water environment and anoxic conditions are key factors in preserving the organic matter found in sediments. Therefore, for either marine shale gas

or continental shale gas, an original sedimentary environment of the shale is where pores can be found saturated with water.

Shale is usually deposited in an aqueous environment. In the original sedimentary environment, therefore, its original pores are saturated with liquid moisture. For the primary pores of inorganic minerals and organic particles (such as intergranular pores formed by the accumulation of particles), as a reservoir settles, the pores undergo a compaction process and a drainage process, and the water is discharged mainly because the pore volume becomes smaller. Therefore, moisture remains in the original pores. During the early accumulation process of organic and inorganic particles, although water can be discharged in a large amount during the compaction and drainage stage, there is actually a decline in porosity during this process. The drainage of water is caused by the compaction of pores. Thus, in the early stage of shale deposition, the water saturation in the pores is high. Only when the organic matter in the shale begins to generate hydrocarbons will the water in the pores be gradually displaced by liquid or gaseous hydrocarbons, and the water saturation will be reduced accordingly.

2.2.1 Water Storage in Organic Pores

As organic matter generates hydrocarbons, the fluids found in shale pores will gradually transition from the original state of "saturated by water" to "gas-water two phases". In different thermal evolution stages, the pore development level and the fluid characteristics in the organic pores are also different. According to the division scheme of Tissot (1984): When 0.5% < Ro < 0.7%, the source rock is at a low maturity stage, mainly producing biogenic gas. When 0.7% < Ro (vitrinite reflectance) < 1.3%, the shale is at the peak of oil generation (the oil generation window), mainly producing liquid hydrocarbons. When 1.3% < Ro < 2.0%, liquid hydrocarbons are gradually reduced while gaseous hydrocarbons slowly increase, mainly consisting of wet gas or

condensate gas (oil) (wet gas window). When Ro > 2.0%, the source rock mainly produces gaseous hydrocarbons such as methane (dry gas window).

Here, we focus primarily on the mature and over-mature stages of shale organic matter evolution (such as Ro>1.3%, gas generation stage), because it is at these stages that shale gas begins to be generated. Generally, organic pores (stoma or kerogen pores) are produced by the escape of bubbles formed by a mixture of liquid hydrocarbons and gaseous hydrocarbons in diagenetic layers when kerogens are converted to hydrocarbons. The major space for gas adsorption in shale are provided by such organic pores. The gas and water storage characteristics in these pores are directly controlled by the number and distribution of polar groups (such as oxygen-containing functional groups). Kerogen pores with polar functional groups exhibit water-wet characteristics, and water molecules tend to form water clusters near the functional groups, coexisting with hydrocarbon molecules in the pores. Kerogen pores without functional groups show non-water-wet characteristics. That is, the pores will repel water molecules, leaving mainly hydrocarbon molecules inside the pores.

Indeed, the property and content of hydrophilic functional groups (mainly oxygen-containing functional groups) of kerogen are in connection with the maturity of kerogen (Ungerer, 1990). As a burial depth increases, temperature and pressure also increase, resulting in the thermal cracking of kerogen structures. In this process, oxygen atoms are gradually removed in the form of H_2O, CO, and CO_2, and the remaining oxygen mostly presents as functional groups. Unfortunately, there have not been studies which directly quantify the functional groups in different types of kerogen during thermal evolution. However, it is certain that with an increase in maturity, kerogen pores will gradually change from hydrophilic pores to hydrophobic pores.

2.2.2 Water Storage in Inorganic Pores

Moisture storage characteristics inside inorganic pores are quite different. Inorganic mineral surfaces usually exhibit strong hydrophilicity. Especially for clay minerals pores, water molecules and clay particles can be tightly combined through hydrogen bonding, electrostatic forces and intermolecular forces. Thus, the moisture in clay minerals are not ignorable. This study takes clay minerals as an example to study the water saturation in inorganic pores.

Considering that shale is usually deposited in a water environment, inorganic pores are mainly dominated by a continuous water phase under original conditions. Along with shale deposition and the thermal evolution of organic matter to generate hydrocarbons, inorganic pores mainly undergo two main drainage stages: compress drainage and hydrocarbon displacement. In the compress drainage stage, the drainage of water is because of a pore volume decrease under overburden pressures. Therefore, the inorganic pores still have a lot of remaining water, and hence maintain a high moisture content. In the hydrocarbon displacement stage, the moisture content in the inorganic pores depends on the capability of hydrocarbon production and the stages of thermal evolution.

At the peak of hydrocarbon generation (mainly producing dry gas), gas pressure continuously increases, and small inorganic pores are further displaced by the gas phase. At this time, a reservoir has a low moisture content, with the bound moisture existing in corners and pore walls. It is worth noting that the high maturity stage corresponds to a high reservoir temperature so the liquid moisture vaporizes into gaseous water in large quantities. When dry gas is injected from organic pores to inorganic pores, the dry gas will carry the gaseous water, which will further reduce the water saturation in the reservoir. The process of evaporation may cause an ultra-low water saturation phenomenon, which will be further discussed in Section 2.3.

2.3 The Ultra-low Water Saturation

2.3.1 Definition

Under original conditions in shale reservoirs, there always exists initial water saturation. Although shale generally contains water, high-quality shale gas wells have very low water production or even no reservoir water production in a gas production process. Such shale gas reservoirs are in an ultra-low water saturation state. That is, initial water is at an immobile state rather than a mobile state.

Bennion (2000) defined the concept of ultru-low initial water saturation. In such a state, the initial water saturation is below the bound water saturation measured by common displacement experiments, where the bound water adsorbs on a pore surface, the non-flowing water is stored in pore corners, and the permeability of the wetting phase (i.e., water phase) is zero. In addition, based on a reservoir capillary-pressure curve, Bennion (2005) further described this concept as such: the original water saturation in a reservoir is lower than that derived from the conventional capillary pressure curve, as shown in Figure 2-1.

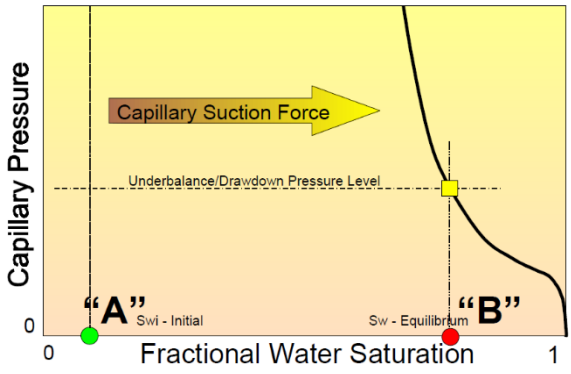

Figure 2-1 Capillary-pressure curve under ultra-low water saturation (Bennion and Thomas, 2005)

This concept is further explained from a micro perspective by Newsham (2003, 2004), as shown in Figure 2-2. In stage (a), a pore is blocked by liquid water, and the Y-Laplace equation can be applied to calculating the difference between gas pressure and liquid pressure. With the

moisture content declining, the liquid phase gradually changes from "slug-like" to "film-like" in stage (b), and the Y-Laplace equation is still applicable for characterizing the pressure difference. When the water film thickness gradually becomes thinner, the surface interactions between the solid surface and the water film cannot be ignored. So, in stage (c), surface interactions on the solid surface need to be considered for the calculation of the gaseous phase/ aqueous phase pressure difference. When the water film further evaporates and turns to discrete water molecules, as shown in stage (d), the Y-Laplace equation is no longer applicable and the pressure difference needs to be characterized by the Kelvin equation (thermodynamic equation). Therefore, in stages (a) and (b), the water saturation and capillary pressure conform to conventional capillary-pressure curves. But in stages (c) and (d), the Kelvin equation is more appropriate instead of the Y-Laplace equation for characterizing the water saturation at an ultra-low water saturation state.

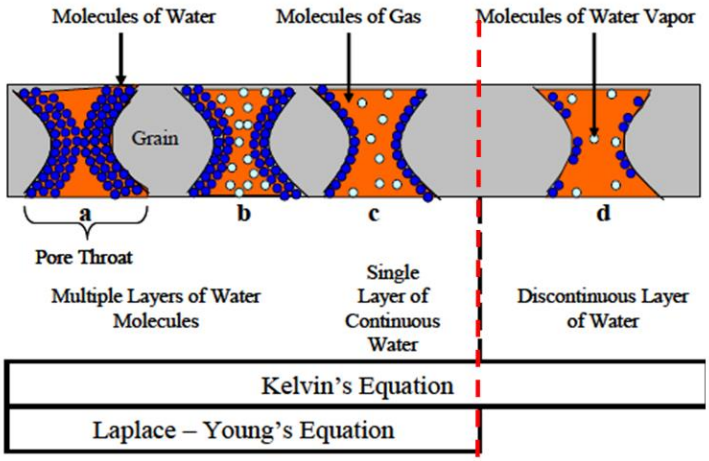

Figure 2-2 Schematic of gas-water relationship for unconventional reservoirs (Newsham et al., 2003, 2004)

2.3.2 Causes

Based on the above research, there are two main ways to form water saturation in a gas reservoir: (i) under the influence of a hydrocarbon expulsion pressure, the water phase is displaced by the gas phase (pressure difference driven displacement); (ii) under the control of the natural gas

humidity, the water phase gradually evaporates (a liquid evaporation process). For conventional reservoirs, the liquid water displacement during oil and gas charging and migration forms the original water saturation; but for a shale gas reservoir, the liquid phase evaporation effect results in an ultra-low water saturation state.

(i) Pressure difference driven displacement

Initially, moisture occupies the inorganic pores. As the gas from organic pores continues to go outward into the inorganic pores, a gas-water pressure difference gradually increases, and the water saturation in inorganic pores decreases. Eventually, it forms a film of bound water, as given by Figure 2-3.

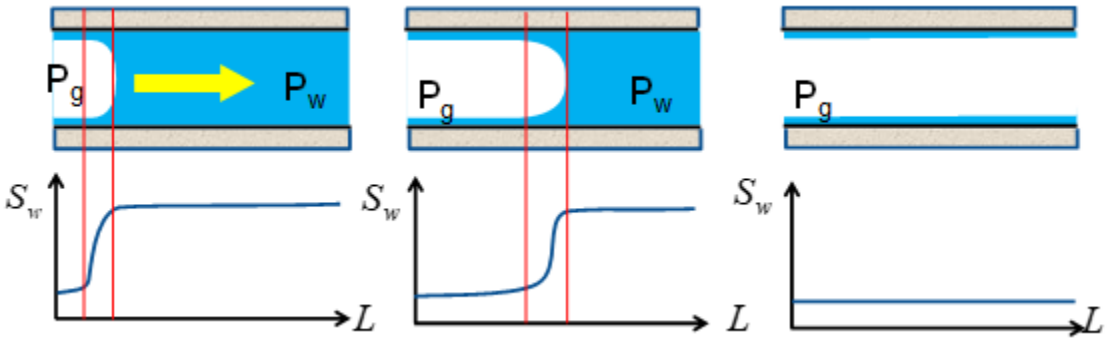

Figure 2-3 Water saturation characteristics during displacement process

The main resistance in this displacement process is the capillary pressure. The formation of water saturation takes a considerable amount of time and can be viewed as an infinitely slow process. For a single ideal pore, in the displacement direction, there is an equilibrium among the gaseous phase pressure P_g, the water phase pressure P_w, and the capillary pressure P_c as shown in Figure (2-4, A):

$$P_g - P_w = P_c = \frac{2\gamma\cos\theta}{r-h} \approx \frac{2\gamma}{r-h} \tag{2.1}$$

where θ is the gas-liquid-solid three-phase contact angle; γ is the air-water surface tension, mN/m. Considering that during the displacement process an inorganic pore wall usually has a water film, the gas-liquid-solid three-phase contact angle θ will be approximately 0° (Zhou et al., 2013). In addition to the mechanical equilibrium in the displacement direction, there is also a mechanical equilibrium at the gas-water film-solid phase interface to maintain the stability of the water film (Figure 2-4, B).

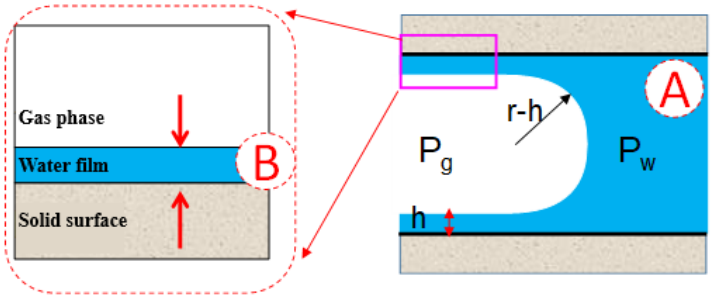

Figure 2-4 Mechanical equilibrium of water film during displacement process

The water film theory shows that (Deryaguin et al., 1987): when the aqueous film on a solid surface is less than 100 nm, the interactions between the liquid-gas interface and the liquid-solid interface become significant, thus maintaining the stability of the water film. This force is called the disjoining pressure. Under the additional force of a wall surface, the structure and mechanical characteristics of the water film near the pore wall surface change, which consequently makes the aqueous film pressure (P_f) not equal to the bulk water pressure (P_w). The pressure difference can be expressed by:

$$P_f - P_w = \Pi(h) \tag{2.2}$$

For an ideal capillary, a water film in pores is not a plane, so the cylindrical capillary pressure caused by the bending of a gas-liquid interface needs to be considered:

$$P_g - P_f = P_c^* = \frac{\gamma}{r-h} \tag{2.3}$$

where *Pc** is the cylindrical capillary pressure in the capillary, MPa.

Therefore, in Figure (2-4, B), the gas phase pressure and water phase pressure have the following relationship:

$$P_g - P_w = \frac{\gamma}{r-h} + \Pi(h) \tag{2.4}$$

where *Π(h)* is disjoining pressure, MPa. The calculation for disjoining pressure will be discussed in Chapter 3.

(ii) Liquid evaporation process

As gaseous hydrocarbons continue to be generated, the dry gas carries water vapor out of a reservoir and the relative humidity of natural gas will decrease. And a bound aqueous film will evaporate, causing the water saturation to be further reduced, as illustrated by Figure 2-5.

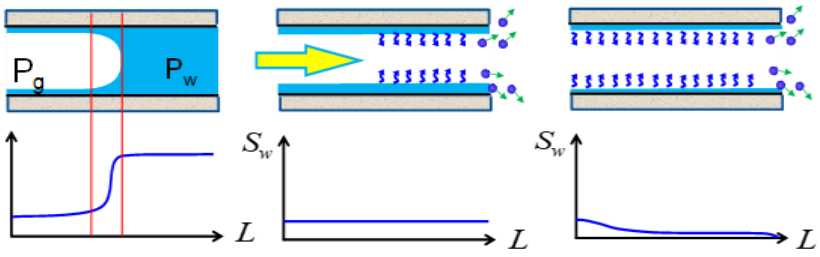

Figure 2-5 Moisture evolution features during evaporation process

For a methane-water vapor mixture, the relative content of water vapor can be expressed by relative humidity *RH*:

$$RH = \frac{P_v}{P_0} \tag{2.5}$$

where P_v is the water vapor partial pressure, MPa; P_0 is the saturated vapor pressure, MPa; *RH* is relative humidity.

Based on the classical Kelvin equation, the natural gas relative humidity (or water vapor partial pressure) when pores are filled with liquid water is related to the curvature of a gas-water interface (or pore radius):

$$\frac{2\gamma\cos\theta}{r} = -\frac{RT}{V_m}\cdot\ln\frac{P_v}{P_0} \tag{2.6}$$

where R is the gas constant, J/(mol·K); V_m is the molar volume of water, cm^3/mol; T is the reservoir temperature, K.

A reservoir is assumed to be a closed system with uniform temperature and pressure. For conventional gas reservoirs, due to a relatively large pore size, the relative humidity of natural gas in the reservoirs is close to 1.0, and the influence of natural gas humidity on the water saturation in pores is basically negligible. By contrast, for shale reservoirs with numerous nanopores and micron-scale pores, the evaporation effect is non-negligible and the relative humidity of natural gas is less than 1.0. In a shale gas reservoir, the relative humidity for the evaporation equilibrium in smaller pores is lower. Thus, when large pores and small pores are in a shale gas reservoir which possess the same humidity, water in large pores will spontaneously move to small pores. Thus, the small pores tend to be blocked by capillary water while large pores tend to have a water film. During this process, the relative humidity of natural gas is playing a non-negligible role in gas/water distributions.

It is worth noting that the classical Kelvin equation only describes the thermodynamic equilibrium after an air-water interface has been formed. The surface interactions and microscopic forces imposed on the aqueous film are not shown in the classical Kelvin equation.

2.4 Summary

(i) This chapter first introduces the various types of pores and fractures in shale reservoirs, which provide a considerable space for methane storage.

(ii) Then we have taken a look at the water saturation in both organic and inorganic pores in shale reservoirs. The water storage characteristics in organic pores are directly controlled by polar functional groups, which are in connection with thematurity of kerogen. With an increase in maturity, kerogen pores gradually change from hydrophilic to hydrophobic. Because shale gas begins to be generated in the mature and over-mature stages (Ro>1.3%), the hydrophobic effect of a kerogen surface will prevent moisture from enter the organic nanopores.

(iii) Inorganic mineral surfaces usually exhibit strong hydrophilicity, with the water molecules and clay particles being tightly combined through various microscopic forces. When the shale reaches the peak of gaseous hydrocarbon generation, gas pressure continuously increases, and inorganic pores are further displaced by the gas phase. The high maturity stage corresponds to a high reservoir temperature, so the liquid water will evaporate into a gas phase and will then be carried away during the injection of dry gas from the organic pores to the inorganic pores, which will further reduce the water saturation in a reservoir and thus cause an ultra-low water saturation phenomenon.

(iv) In regard of the pressure difference driven displacement, the mechanical equilibrium in the displacement direction is maintained by the capillary pressure, which is characterized by the Y-Laplace equation. And the disjoining pressure should also be considered to maintain the stability of a liquid film at a gas-water film-solid interface. In regards to the liquid evaporation process, the classical Kelvin equation characterizes the relative humidity using the curvature of a gas-water interface, but the interactions between a pore surface and an aqueous film, and the effective pore diameter deduction are not shown in the classical Kelvin equation.

Chapter 3 Mathematical Model of Water in Shale Clay Pores

Considering the sub-irreducible water saturation state of shale reservoirs, the moisture distribution features are controlled by thermodynamic equilibrium. We first focus on the thermodynamic equilibrium found in typical shale inorganic pores, such as clay pores. Then, based on the water film theory (the DLOV theory, i.e., Derjaguin-Landau-Verwey-Overbeek theory), we consider microscopic forces between clay, a water film, and the gas phase and then establish a mathematical model for calculating the water distribution in nano-scale pores.

3.1 Thermodynamic Equilibrium Analysis

The assumptions for the mathematical model of water film thickness in nano-scale pores are as follows: (1) There are only two components in the gas phase : methane and water vapor; (2) the surfaces of the shale's inorganic pores are hydrophilic and mainly adsorbs water molecules (i.e., the adsorbed methane is ignored); (3) a water film is a rigid fluid and its compressibility is negligible; (4) dissolution of methane in the water film is ignored; (5) the equilibrium process of this system is an isothermal process; (6) the interaction potential of a pore wall surface is homogeneously distributed, and thus the liquid water film is homogeneous and equal in thickness; (7)the gas phase of the reservoir is a continuous phase, with a unified temperature, pressure and humidity.

In this section, we first analyze a gas/water/solid interaction on a flat surface. The thermodynamic equilibrium is shown in Figure 3-1. Taking a mole of gaseous water molecules as an example, the water molecules in the gas phase produce a liquid film on the solid surface through adsorption; its thickness is h in such a gas-liquid (water film)-solid (shale clay) three-phase thermodynamic equilibrium.

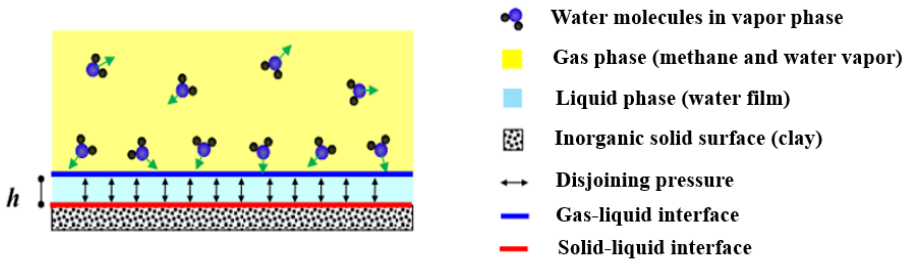

Figure 3-1 Shale-water-gas thermodynamic equilibrium

From a thermodynamic point of view, a chemical potential change (adsorption potential) for per molar water vapor to be adsorbed to form a water film is expressed as (Grant and Manes, 1066):

$$\Delta\mu_1 = \int_{P_v}^{P_0^*} \frac{RT}{P} dP = -RT \ln \frac{P_v}{P_0^*} \tag{3.1}$$

where P_0* is the saturated vapor pressure of the water film, MPa; P_v is the partial pressure of water vapor, MPa.

In this mixed system, the saturated vapor pressure P_0* of the aqueous film can be described by Raoult's law (Koga, 2017) as:

$$P_0^* = P_0 \cdot x_A \tag{3.2}$$

where P_0 is the saturated vapor pressure of pure water, MPa; x_A is the mole fraction of pure water in the water film.

Ignoring the dissolved methane in water film (i.e., $x_A = 1$), the saturated vapor pressure of the liquid film equals the saturated vapor pressure of pure water:

$$P_0^* = P_0 \tag{3.3}$$

Using equation (3.1) and equation (3.3), the chemical potential change of per mole of water vapor to turn to per mole of liquid water through adsorption can be expressed as:

$$\Delta\mu_1 = \int_{P_v}^{P_0^*} \frac{RT}{P} dP = -RT \ln \frac{P_v}{P_0} \tag{3.4}$$

where Pv / P_0 is the relative humidity of natural gas, which can be expressed by *RH*.

At the same time, from a mechanical point of view, the reason that water molecules are able to form a stable water film is due to a solid-water film-gas interaction. Considering that a solid surface imposes a force on the water vapor through a water film, this interaction acts between two interfaces, including a solid-liquid interface and a gas-liquid interface. Assuming the water film thickness to be *h* during adsorption process, the interaction forces between solid, liquid and gas are characterized by the disjoining pressure. Then the work (or energy change) caused by disjoining pressure $\Pi(h)$ in this adsorption process can be expressed as:

$$\Delta\mu_2 = \Pi(h) \cdot A_f \cdot h \tag{3.5}$$

Where *h* is the thickness of the clay bound liquid film, nm; A_f is the surface area of the water film, m^2.

When per mole of water vapor adsorbs to produce a water film, the water film thickness is expressed by:

$$h = \frac{V_m}{A_f} \tag{3.6}$$

where V_m is the molar volume of water, 18 cm^3/mol.

Through equation (3.6) and equation (3.5), we get:

$$\Delta\mu_2 = \prod(h) \cdot V_m \tag{3.7}$$

Both $\Delta\mu_1$ and $\Delta\mu_2$ describe the process of per molar water vapor turning into a water film. $\Delta\mu_1$ describes the chemical potential change of the water film from the perspective of thermodynamics, and $\Delta\mu_2$ describes the change of free energy of the water film by disjoining pressure from a mechanical point of view; the free energy change is equal to the chemical potential change, and thus $\Delta\mu_1$ is equal to $\Delta\mu_2$. Combining equation (3.4) and equation (3.7), under the equilibrium of solid-water-gas interactions, we can obtain:

$$\prod(h) \cdot V_m = -RT \ln \frac{P_v}{P_0} \tag{3.8}$$

3.2 Surface Force and Disjoining Pressure

In this study, a surface force interaction (disjoining pressure, the DLOV theory) is characterized by a method proposed by Derjaguin (1987). In this model, disjoining pressure is composed of three parts: an intermolecular force (Π_m), an electrostatic force (Π_e), and a structural force (Π_{st}). All these three parts have a corresponding relationship with the water film thickness h:

$$\Pi(h) = \Pi_m(h) + \Pi_e(h) + \Pi_{st}(h) \tag{3.9}$$

3.2.1 Intermolecular Force

Intermolecular forces mainly consist of short-range forces (i.e. London force, Keeson force and Debye force) and long-range forces, formed by the intermolecular transmission of the short-range forces (Starov et al., 2007). A force can be either an attraction or a repulsion, depending on the nature of a solid surface.

Coupling the short-range and long-range forces between various molecules, the intermolecular forces is described as (Starov et al., 2007):

$$\Pi_m(h) = \frac{A_H}{h^3} \tag{3.10}$$

where A_H is the Hamaker constant, J. Takahashi and Kovscek (2010) indicated that A_H for a clay-water-gas interaction should be around 1.0×10^{-20} J and, therefore, this value is also adopted in our study.

3.2.2 Electrostatic Force

When the interacting surfaces have certain electric charges, a coulomb force, also known as an electrostatic force, will be generated between the surfaces. The number of charges on the interacting surfaces influences the magnitude of the electrostatic force, and the electric polarities of the surfaces can control its direction. A clay surface is usually negatively charged. Although in their original state water molecules are electroneutral, as polar molecules, they are easily polarized by the charges near them. The electrostatic force between two planes is roughly given by (Starov et al., 2007):

$$\Pi_e(h) = \frac{\varepsilon\varepsilon_0}{8\pi}\frac{(\zeta_1 - \xi_2)^2}{h^2} \tag{3.11}$$

where ε_0 is the vacuum dielectric constant, which is 8.85×10^{-12} F/m; ε is the relative dielectric constant of liquid water, which is 81.5; ζ_1 and ζ_2 are the electric potentials of the two interacting surfaces; ζ_1 - ζ_2 is the electric potential difference, mV. In this research, the two interacting surfaces are water-methane interface and clay-water interface; thus ζ_1 - ζ_2 is approximately 40~80 mV (Churaev, 1995). This electrostatic force acts as an attraction.

3.2.3 Structural Force

Under the impact of the polarity or electric charges of the solid surface, polar molecules (such as water molecules) near the solid surface will be aligned to form a transition layer. The molecular structure in a transition layer is different from that in the bulk phase, which will affect the adsorption of other molecules to a certain extent. This force is called a structural force (Derjaguin et al., 1987). Previous studies (Churaev,1995; Takahashi and Kovscek, 2010) have shown that the structural force generally belongs to a kind of short-range force with the interaction distance of less than 5nm (here the interaction distance equals the water film thickness). This structural force can be either an attraction or a repulsion (Derjaguin et al., 1987). If the contact angle formed by the solid phase and the liquid phase is less than 25°, the structural force will appear as a force of attraction.

Owing to the hydrogen bond of water molecules and the charged clay surface, water molecules near a clay surface will be aligned and form 'clay bound water', consequently affecting the adsorption capacity of the clay surface. Considering that the wetting angle between clay and water is generally less than 20°, the bound water on the clay surface will act as an attraction and promote the adsorption of water. A semi-empirical equation is adopted to express the structural force (Jahediesfanjani, 2007):

$$\prod_s(h) = ke^{-\frac{h}{\lambda}} \tag{3.12}$$

where k is the structural force coefficient, which is generally fitted through experiments, N/m^2, and λ is the characteristic length of water molecules, nm. A value of k is determined by the wettability of a clay surface in a clay-water-gas three-phase system. Churaev (1995a, b) found that when the contact angle is smaller than 20°, the structural force will appear as a hydrophilic

attraction (k>0);and with the contact angle being above 40°, the structural force will appear as a hydrophobic repulsion (k <0). However, when the contact angle is between 20° and 40°, the structural force can be ignored altogether. In our research, the clay surface is strongly hydrophilic, so the k and λ values used for calculations in our study are: λ =1∼2 nm, k =1×10^{-7} N/m^2 (Churaev, 1995a, b).

To sum up, by combining equations (3.8)-(3.12), the mathematical relation between natural gas humidity and liquid film thickness is:

$$\Pi(h) = \Pi_m(h) + \Pi_e(h) + \Pi_{st}(h) = -\frac{RT}{V_m}\ln\frac{P_v}{P_0} \tag{3.13}$$

3.3 Slit Pore and Capillary Models

In actual shale samples, the various shale pores can be simplified into two categories: slit pores and capillaries. In actual shale reservoirs, there are also square and triangular pores, both of which are similar to capillaries. Thus, we only conduct our research on the slit pores and capillaries.

3.3.1 Slit Pore Model

Kaolinite, montmorillonite and illite are the common clay minerals in shale include. These minerals generally have a crystal layer structure, and pores between their crystal layers are generally slit-shaped. In addition, according to the EMG scans at high magnification of shale clay pores, clay nanopores exhibit characteristics that are similar to slit pores and the slit width is mainly between 3 and 20 nm (Crutis et al., 2011).

The thermodynamic equilibrium process of water adsorption in a slit pore is similar to that in a flat surface, and $\Delta\mu_1$ can be expressed by formula (3.6). However, the mechanical equilibrium of an adsorbed water film inside a slit pore is quite different. For mechanical analysis of the

adsorbed water film on a single flat surface, there is only one surface interaction to be considered: the interaction between the single flat surface and its adsorbed water film. Different from a single flat surface, a slit pore has two parallel pore walls with each wall having its own adsorbed water film. So, for the mechanical analysis of the water film on either wall of a slit pore, there are three interactions to be considered: (1) a force between the aqueous film and the pore wall, on which this aqueous film is located, $\Pi_1(h)$; (2) a force between the aqueous film and the opposite wall, $\Pi_2(h)$; (3) a force between the adsorbed aqueous films, $\Pi_3(h)$.

Assuming that the thickness of a liquid film and the width of a pore are h and H, respectively. The total thickness of the liquid film in this pore is 2h with two liquid on both pore walls. Mechanical analyses of the water films in a slit pore are shown in Figure 3-2.

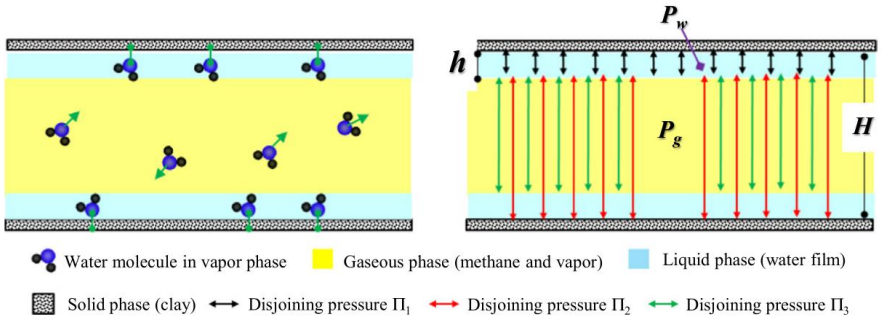

Figure 3-2 Mechanical analysis of aqueous films inside a slit pore

The disjoining pressure is expressed as:

$$\begin{aligned}
&\Pi_{slit}(h) = \Pi_1(h) + \Pi_2(h) + \Pi_3(h) \\
&\Pi_1(h) = \frac{A_H}{h^3} + \frac{\varepsilon\varepsilon_0}{8\pi}\frac{(\zeta_1 - \xi_2)^2}{h^2} + ke^{-\frac{h}{\lambda}} \\
&\Pi_2(h) = \frac{A_H}{(H-h)^3} + \frac{\varepsilon\varepsilon_0}{8\pi}\frac{(\zeta_1 - \xi_2)^2}{(H-h)^2} + ke^{-\frac{H-h}{\lambda}} \\
&\Pi_3(h) = \frac{A_H}{(H-2h)^3}
\end{aligned} \tag{3.14}$$

where both long-range forces (intermolecular force Π_m and electrostatic force Π_e) and a short-range force (structural force Π_s) are considered for $\Pi_1(h)$ and $\Pi_2(h)$, MPa; and Π_e and Π_s can be ignored for $\Pi_3(h)$ because there is no electric potential difference between the two liquid films, MPa.

Equations (3.8) and (3.14) can be combined as:

$$P_{slit}(h) = P_1 + P_2 + P_3 = -\frac{RT}{V_m}\ln\frac{P_v}{P_0} \tag{3.15}$$

The water saturation in a single slit pore can be further expressed as:

$$S_{w-slit}(i) = \frac{2h}{H} \tag{3.16}$$

When $\Delta\zeta$ = 50 mV, we calculate the water saturations and liquid film thicknesses and in a slit pore for each given relative humidity with different pore widths. The relationship between natural gas humidity and thicknesses of aqueous films inside slit pores with various sizes, and corresponding water saturations are given in Figure 3-3 and Figure 3-4. The results show that for slit pores, a pore size has little effect on the water film thickness. However, once the water film thickness converts to water saturation, the amount of water saturation found in slit pores differs substantially based on the pore size. Indeed, under the same relative humidity conditions (the reservoir system generally possesses the same temperature, pressure and humidity), smaller pore sizes lead to higher water saturations. A capillary condensation phenomenon in nanopores is also observed. That is, when the relative humidity is less than 1 (RH < 1), the water saturations of some small pores can become 100% ($S_w(i)$ = 100%), which means these pores are blocked by moisture. The capillary condensation phenomenon in smaller pores is more significant.

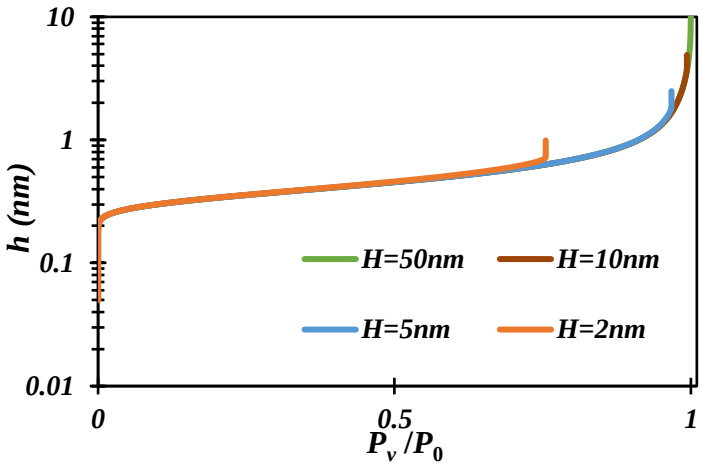

Figure 3-3 Aqueous film thickness inside various sizes of slit pores

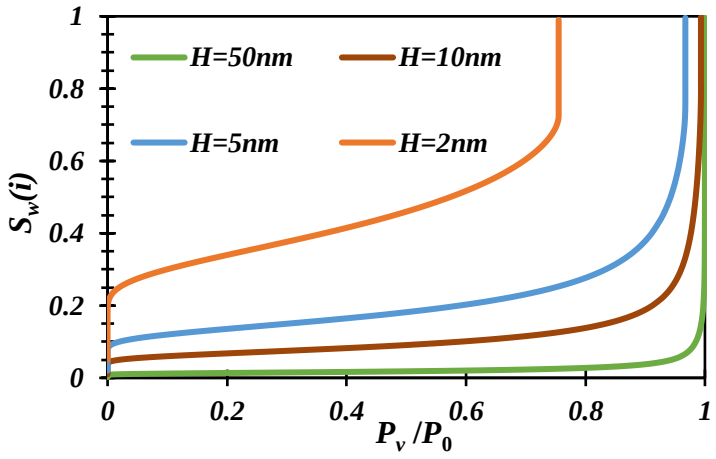

Figure 3-4 Water saturations in various sizes of slit pores

3.3.2 Capillary Model

The thermodynamic equilibrium process of water film adsorption in the capillary model is similar to that on a single flat surface, and $\Delta\mu_1$ can be expressed by equation (3.4). However, the mechanical equilibrium of the liquid film found in the capillary model is different. Since the water film in the capillary is a curved rather than a planar surface, when analyzing the mechanical equilibrium of the curved water film, capillary pressure generated by the water film also needs to be considered. Assume that the diameter of the capillary is *D*; the radius of the capillary is *r*; the

liquid film is evenly distributed on the wall surface of a pore with thickness of *h*, the mechanical analysis of the water film in the capillary has been shown as Figure 3-5.

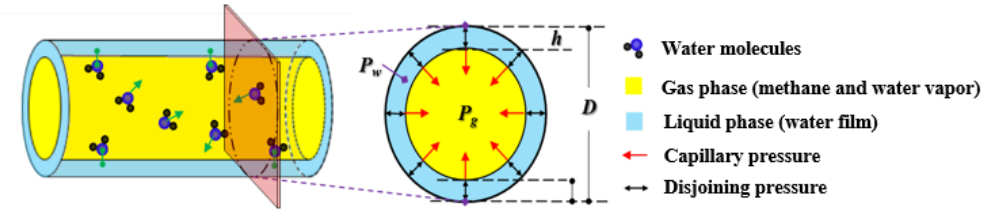

Figure 3-5 Forces imposed on an aqueous film inside a capillary

The force on the water film in the capillary is:

$$\prod_{capillary}(h) = \prod(h) + P_c^* = \prod(h) + \frac{\gamma}{r-h} \tag{3.17}$$

Equation (3.8) and (3.17) can be combined as:

$$\Pi_{capillary}(h) = \prod(h) + \frac{\gamma}{r-h} = -\frac{RT}{V_m}\ln\frac{P_v}{P_0} \tag{3.18}$$

The water saturation can be further expressed as:

$$S_{w-capillary}(i) = 1 - \left(1 - \frac{h}{r}\right)^2 \tag{3.19}$$

When $\Delta\zeta$ = 50 mV, we calculate the water saturations and thicknesses of the aqueous films for each given relative humidity in capillaries with various sizes. The water film thicknesses in capillaries with different sizes are given in Figure 3-6, and corresponding water saturations are shown in Figure 3-7. Through the results we can see that for capillaries, pore size has a significant impact on both water saturations and the thicknesses of liquid films. That is, smaller pore sizes

lead to thicker liquid films and greater water saturations. Moreover, because the pore wall potential of the capillary is stronger than that of a slit pore, the critical relative humidity of the condensation phenomenon in the capillary is lower than that in the slit pore. Therefore, the water film in the capillary is more prone to condensation. A capillary generally has higher water saturation than a slit pore with the same pore size under the same relative humidity.

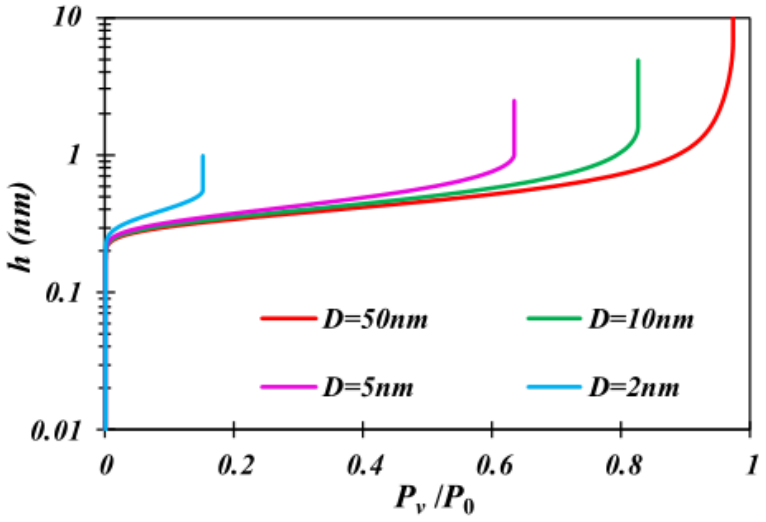

Figure 3-6 Aqueous film thicknesses in various sizes of capillaries

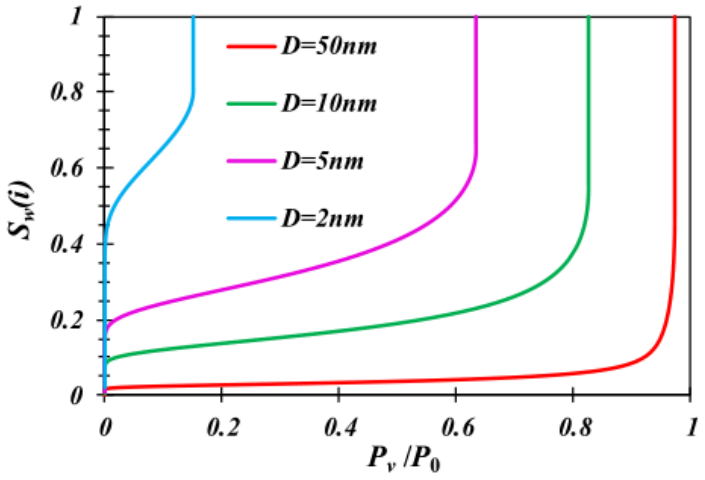

Figure 3-7 Water saturations in capillaries of various sizes

3.4 Summary

(i) Under the sub-irreducible water saturation in shale formations, the adsorption-evaporation thermodynamic equilibrium has been analyzed and shown to be the main factor that influences the water distribution in a reservoir. By considering the disjoining pressure and microscopic forces, we have established a mathematical model for calculating the thicknesses of liquid films in shale clay pores. Taking a pore shape into consideration, the established model is divided into slit pore and capillary cases.

(ii) The water saturation and aqueous film thickness, inside a slit pore and inside a capillary, under different relative humidity, are calculated when the pore width is 2nm, 5nm, 10nm and 50nm, respectively. For slit pores, a pore size has little effect on the water film thickness. However, once the water film thickness converts to water saturation, water saturations found in different sizes of slit pores differ substantially. Smaller pore sizes lead to higher water saturations under the same relative humidity. For capillaries, smaller pore sizes lead to thicker water films and higher water saturations.

(iii) Owing to the effect of the pore-wall potential, the capillary condensation phenomenon in nanopores is observed, especially in pores smaller than 5 nm. That is, the micro-pores can be completely filled with water ($S_w(i) = 1$) when the relative humidity is less than 1. Based on our calculation results, the wall potential is mainly influenced by a pore size and pore shape. For either a slit pore or capillary, the capillary condensation phenomenon in smaller pores is more significant. For pores with the same pore size (slit width or capillary diameter), the wall potential of the capillary is greater than that of the slit pore. That is, capillaries have higher water saturations and thicker wetting films than slit pores of the same pore sizes, and thus the condensation phenomenon is more likely to happen in capillaries.

Chapter 4 Mathematical Model for Methane Adsorption in Shale Clay Pores

This chapter will focus on inorganic pores to study gas adsorption in them. Under original shale reservoir conditions, these strongly hydrophilic pores generally contain water. Thus, we focus on the mechanism of a gas-liquid-solid three-phase interaction that is found especially in clay pores.

4.1 Gas-solid Adsorption

4.1.1 Gas-solid Adsorption Theory

Under dry conditions, the London dispersion force, which is a type of physical adsorption, is the leading driving force for gas adsorption on a clay surface. Indeed, according to experimental data (Ji et al., 2012; Ross and Bustin, 2008, 2009), the maximum adsorption amount is linearly dependent on the specific surface area (Figure 4-1):

$$n_{max-dry} = KA \tag{4.1}$$

where K characterizes the maximum adsorption per surface area of the gas-solid interface, mmol/g; A is the specific surface area of clay, m^2/g; $n_{max\text{-}dry}$ is the maximum adsorption amount of methane under dry conditions, mmol/g. The fitting results in Figure 4-1 show that: K = 0.0041-0.0088 $mmol/m^2$. In the research of (Ji et al., 2012), K=0.0053 $mmol/m^2$, so this value will also be used in our calculations.

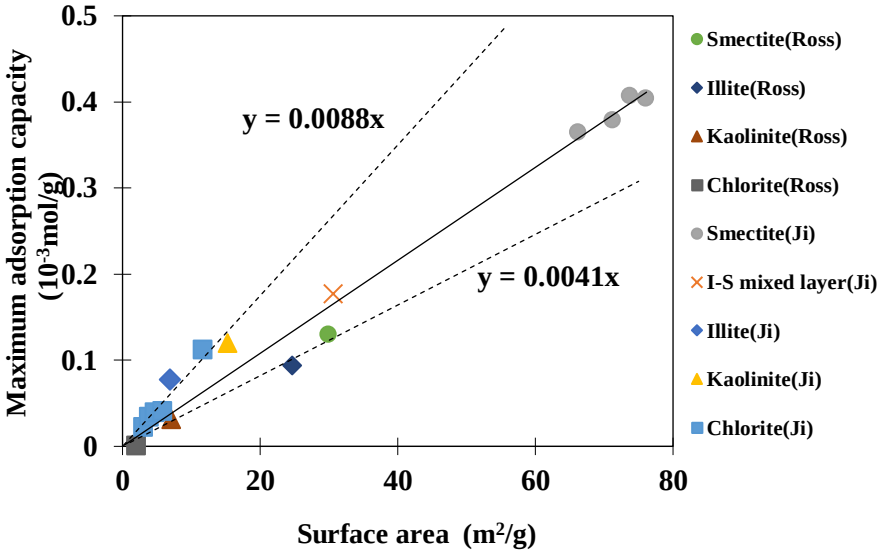

Figure 4-1 Maximum adsorption capacity vs. surface area of clay (Ross and Bustin, 2008, 2009)

Under dry conditions, the gas adsorption is calculated through the Langmuir equation at a gas-solid interface (Langmuir, 1917), which is

$$n_{ad-dry} = K \cdot A_{slit} \frac{P}{P + P_L} \tag{4.2}$$

where $n_{ad\text{-}dry}$ is the amount of adsorbed methane under dry conditions, mmol/g; P_L is the Langmuir pressure (gas-solid). The value of P_L varies with clay mineral type and temperature, ranging from 2 to 8 MPa; P_L of montmorillonite is between 2 - 4 MPa; P_L of illite and kaolinite is between 5 - 8 MPa (Ji et al., 2012). Knowing that there are a variety of complex shapes of interlayer spacing and inter-granular pores found in shale clay, we will conduct our research based on a slit pore model and a capillary model.

4.1.2 Adsorption in Slit Pores

Under a gas-solid interaction, Figure 4-2 displays the methane adsorption model in a slit pore.

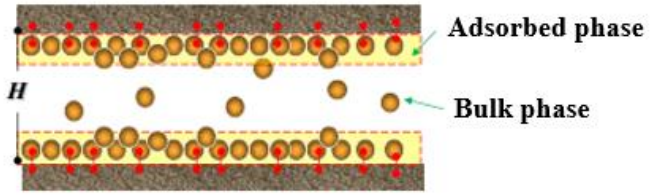

Figure 4-2 Methane–clay adsorption schematics inside a slit pore

A slit pore has two layers so the surface area is $2A_{slit}$. The interlayer spacing is H. Therefore, the methane adsorption amount ($n_{ad\text{-}dry\text{-}slit}$) in a slit pore is given by:

$$n_{ad-dry-slit} = 2 \cdot K \cdot A_{slit} \frac{P}{P + P_L} \tag{4.2}$$

4.1.3 Adsorption in Capillaries

Under a gas-solid interaction, Figure 4-3 gives the adsorption model in a capillary.

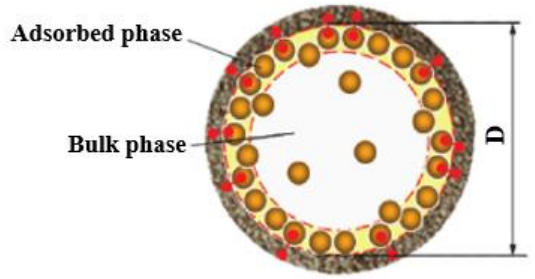

Figure 4-3 Methane–clay adsorption schematics inside a capillary

We assume that the surface area of the capillary is $A_{capillary}$. The diameter and the radius of the capillary are D and r, respectively. Thus, the methane adsorption amount in a capillary ($n_{ad\text{-}dry\text{-}capillary}$) is be given by:

$$n_{ad-dry-capillary} = K \cdot A_{capillary} \frac{P}{P + P_L} \tag{4.3}$$

4.2 Gas-liquid Adsorption

4.2.1 Gas-liquid Adsorption Theory

At present there are few experimental and theoretical studies related to methane adsorption on a wetted surface of clay pores, so the volatile organic compounds (VOCs) adsorption theory on the surface of soil pores will be used. According to the soil adsorption theory (Ho and Webb, 2006), when an aqueous film is formed on the soil surface, there exist: (i) dissolution of organic gas in the water film; (ii) adsorption of organic gas on the liquid film (gas-liquid interface adsorption); and finally, (iii) adsorption of the dissolved organic gas on the soil surface (liquid-solid interface adsorption).

In cases (i) and (ii), whether the organic gas dissolves in the water film or adsorbs on the surface of the water film depends on its solubility (Costanza and Brusseau, 2000). For example, trichloroethylene, which has a relatively high solubility (under normal temperature and pressure) of 1,000 mg/L, is mainly dissolved in the water film, while paraxylene, which has a relatively low solubility of 198 mg/L, is mostly adsorbed on the water film surface. Given that methane has extremely low solubility in water, methane primarily adsorbs on the water film. In case (iii), because clay is highly hydrophilic, when methane molecules and water molecules coexist, the surface of clay gets covered by the adsorbed moisture, making it not able to directly adsorb the methane molecules. Therefore, methane adsorption on the wetted clay surface will be in the form of gas-liquid interface adsorption.

In the soil adsorption theory, there are various models for quantifying the gas-liquid interface adsorption of VOCs. Nevertheless, those models only apply to a certain type of organic gas and most of them are semi-empirical equations. The ambient temperature of the VOCs adsorption process is below the critical temperature of VOCs, which means VOCs in a gas phase

can condense into a liquid phase. The adsorption of methane in actual shale reservoirs is fundamentally dissimilar from VOCs adsorption. Besides, when differences in depositional environments of soil and shale are considered, their different pore structures also make the semi-empirical model for the gas-liquid adsorption of VOCs on soil surface less applicable for methane adsorption on a wetted clay surface. Therefore, the Gibbs adsorption method (Kondo et al., 2006) has been selected for our analysis as it is widely applicable for gas-liquid adsorption and more accurately describes the adsorption of methane on clay bound water films. The gas-water adsorption amount and the surface tension have the following relationship:

$$\frac{(\partial\gamma)}{(\partial P)_T} = -\frac{\Gamma RT}{P} \tag{4.4}$$

where P is the gas pressure, MPa; Γ is the amount of adsorbed methane per surface area at the gas-water interface, mol/m^2; γ is the gas-water surface tension, mN/m; T is temperature, K; R is the gas constant, J/mol·K.

If the gas-water interface surface area is A (m^2/g), the relationship between the methane adsorption amount n_{ad-wet} (mmol/g) on wet clay surface and gas pressure P is described as:

$$n_{ad-wet} = \Gamma \cdot A = \left[-\frac{(\partial\gamma)}{(\partial P)_T}\frac{P}{RT}\right] \cdot A \tag{4.5}$$

Experimental data (Jennings and Newman, 1971) has shown how the methane-water surface tension changes with gas pressure at various temperatures, as shown in Figure 4-4. We use equation (4.7) to fit the surface tension-pressure relationship:

$$\gamma = a\ln(b+P) + c \tag{4.6}$$

where a, b and c are fitting parameters. See Table 4-1 for the values of these parameters under different temperatures.

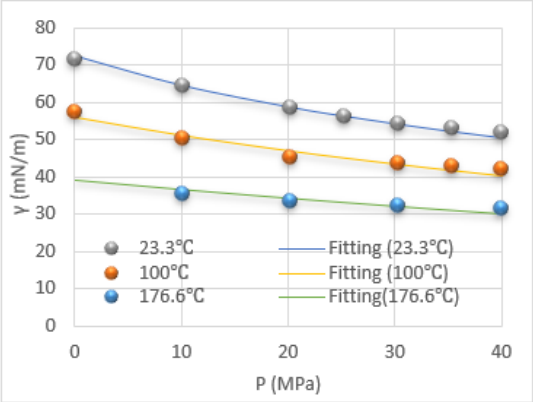

Figure 4-4 Methane-water surface tension vs. pressure

Table 4-1 Fitting equations and parameters for gas-water surface tension

Temperature	*a*	*b*	*c*	Fitting equation
23.3℃	-21.41	22.28	139.0	γ=-21.41×ln(22.28+P) +139
100℃	-26.79	50.13	161.0	γ=-26.79×ln(50.13+P) +161
176.6℃	-32.29	120.22	194.0	γ=-30.91×ln(120.22+P) +194

Combining equation (4-7) and equation (4-6), the amount of adsorbed methane has a certain relationship with gas pressure:

$$n_{ad-wet} = \frac{aA}{RT}\frac{P}{P+b} = \Gamma^* \cdot A \cdot \frac{P}{P+P^*} \tag{4.7}$$

where Γ^* is the maximum adsorbed gas amount per surface area at the gas-water interface, mmol/ m^2; P^* is the Langmuir pressure (gas-liquid), MPa. Calculated from the fitting parameters in Table 4-1, Γ^* is 0.008 64 mmol/m^2 and its vlue does not change with temperature, while the value of P^* is 22.28, 50.13, 120.22 MPa, at a temperature of 23.3℃, 100. 0℃, 176.6 ℃, respectively.

Using only equation (4.7) to fit the relationship between methane-water surface tension and gas pressure, the derived equation (4.8) conforms to the Langmuir adsorption equation. If other formulas (such as polynomials) are used instead of equation (4.7) to fit the surface tension-gas pressure relationship, equation (4.8) will also change.

4.2.2 Adsorption in Slit Pores

Under a gas-liquid interaction, the methane adsorption model in a slit pore is given by Figure 4-5.

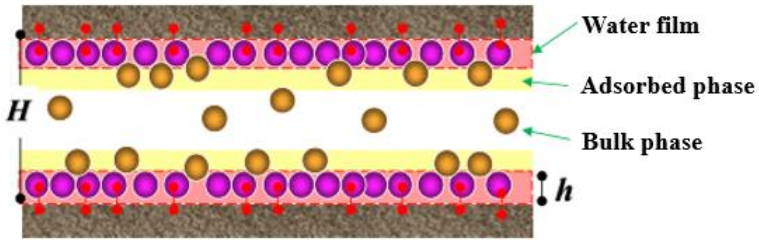

Figure 4-5 Methane-water adsorption schematics inside a slit pore

The thin wetting film is assumed to be of uniform thickness, so the methane adsorption amount in a slit pore can be expressed by:

$$n_{ad-wet-slit} = 2A_{slit} \cdot \Gamma^* \cdot \frac{P}{P + P^*} \tag{4.8}$$

4.2.3 Adsorption in Capillaries

Under a gas-liquid interaction, the methane adsorption model in a capillary is shown in Figure 4-6. In the capillary model, as the liquid film thickness (water saturation in the pore) increases, the effective surface area for the adsorption of methane gradually decreases. That is, the capacity of adsorption drops as water saturation rises.

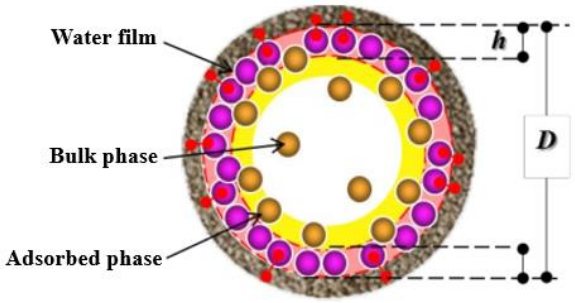

Figure 4-6 Methane-water adsorption schematics inside a capillary

The water saturation in a capillary can be expressed by:

$$S_{w-capillary}(i) = \frac{r^2 - (r-h)^2}{r^2} \tag{4.9}$$

where h is the thickness of the liquid film; r is the capillary radius.

The effective surface area for the adsorption of methane is:

$$A_{eff} = A_{capillary} \cdot \sqrt{1 - S_w} \tag{4.10}$$

where $A_{capillary}$ is the surface area of a capillary.

The methane adsorption amount in a capillary can be expressed by:

$$n_{ad-wet-capillary} = A_{capillary} \cdot \sqrt{1 - S_{w-capillary}(i)} \cdot \Gamma^* \cdot \frac{P}{P + P^*} \tag{4.11}$$

4.3 Gas-liquid-solid Adsorption

Decades ago, research (Ong and lion, 1991) showed that when the moisture adsorbed on the soil surface is between 0 and 1 layer, there is strong competition between gaseous trichloroethylene molecules (TCE) and water molecules to adsorb on a soil surface. Indeed, when there is more than monolayer water molecules, TCE is adsorbed on a water film and interacts with water molecules.

Drawing lessons from these research results, we use the thickness of a single layer of water molecules (0.4 nm) as a critical value. Therefore, when the surface of clay is covered with at least monolayer of water molecules, the long-range force imposed on methane molecules by the clay surface is much smaller than the short-range force imposed on methane molecules by water molecules. Thus, the methane adsorption belongs to gas-liquid interface adsorption. Additionally, while the solid surface has not been completely covered by moisture, part of surface area can be occupied by methane molecules, which is given by Figure 4-7.

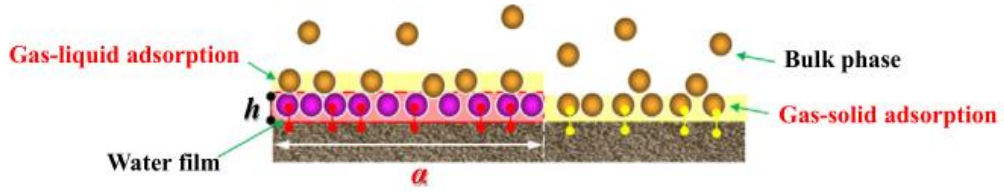

Figure 4-7 Methane–moisture-clay interactions schematics on the surface of clay

We define α as the water coverage coefficient:

$$\alpha = A_{H_2O} / A_{total} \tag{4.12}$$

where A_{H_2O} is the area of the water-covering clay surface, m^2; A_{total} is the total surface area of clay, m^2.

Under a gas-liquid-solid three-phase interaction, the methane adsorption capacity can be expressed as:

$$n_{ad-mix} = (1-\alpha) \cdot n_{ad-dry} + \alpha \cdot n_{ad-wet} \tag{4.13}$$

4.3.1 Adsorption in Slit Pores

In a slit pore case, when there is exactly one single layer of water molecules covering a pore wall, the water saturation in a pore (S_{mon}) is:

$$S_{mon} = \frac{2 \times 0.4}{H} \tag{4.14}$$

where H is the interlayer spacing; 0.4 is thickness of a single layer of water molecules (0.4 nm).

For the calculation of the water coverage coefficient, we assume that the adsorbed moisture is homogeneously distributed on the clay surface. Then, the water coverage coefficient can be expressed as:

$$\alpha = \frac{S_w}{S_{mon}} \tag{4.15}$$

Thus, the methane adsorption amount in a slit pore can be described as:

$$\begin{cases} n_{ad-dry-slit} = 2A_{slit} \cdot K \cdot \dfrac{P}{P+P_L} \\ (S_w = 0) \\ n_{ad-mix-slit} = \alpha \cdot n_{ad-dry-slit} + (1-\alpha) n_{ad-wet-slit} \\ (0 \le S_w \le S_{mon}) \\ n_{ad-wet-slit} = 2A_{slit} \cdot \Gamma^* \cdot \dfrac{P}{P+P^*} \\ (S_{mon} < S_w < 1) \end{cases} \tag{4.17}$$

4.3.2 Adsorption in Capillaries

In a capillary, with a pore surface occupied by a single layer of moisture, the water saturation S_{mon} is:

$$S_{mon} = \frac{r^2-(r-0.4)^2}{r^2} \tag{4.16}$$

where r is the capillary radius; 0.4 is thickness of a single layer of water molecules (0.4 nm).

The water coverage coefficient can also be calculated by equation (4.16). The methane adsorption amount in a capillary is:

$$\begin{cases} n_{ad-dry-capillary} = A_{capillary} \cdot K \cdot \dfrac{P}{P+P_L} \\ (S_w = 0) \\ n_{ad-mix-capillary} = \alpha \cdot n_{ad-dry-capillary} + (1-\alpha) n_{ad-wet-capillary} \\ (0 \le S_w \le S_{mon}) \\ n_{ad-wet-capillary} = A_{capillary} \cdot \sqrt{1-S_{w-capillary}(i)} \cdot \Gamma^* \cdot \dfrac{P}{P+P^*} \\ (S_{mon} < S_w < 1) \end{cases} \tag{4.19}$$

It is worth noting that for equation (4.17) or equation (4.19), the type of gas-liquid-solid interaction is determined by the water coverage coefficient α, and this value is directly determined

by the water film thickness. The calculation methods for water film thickness in both slit pores and capillaries have been provided in Chapter 3.

4.4 Model Validation

We used the molecular simulation data in 4 nm pores (Jin, 2014) to validate the proposed model.

4.4.1 Basic Parameters

The basic calculation parameters are shown in Table 4-2, where the molecular simulation temperature is T = 298 K; K = 0.0075 mmol/m^2, P_L = 2.5 MPa (Jin, 2013); based on the fitting parameters for gas-water surface tension in Table 4-1, Γ^* = 0.00864 mmol/m^2, P^* = *22.28 MPa*.

Table 4-2 Basic parameter for methane adsorption

Parameter	*Symbol (unit)*	*Value*
Temperature	*T (K)*	*298*
Pressure	*P (MPa)*	*0~40*
Pore size	*H (nm)*	*4*
Maximum adsorption capacity per unit area (gas-solid)	*K (mmol/m^2)*	*0.0075*
Langmuir pressure of the gas-solid interface	*P_L (MPa)*	*2.5*
Maximum adsorption capacity per unit area (gas-liquid)	*Γ^* (mmol/m^2)*	*0.00864*
Langmuir pressure of the gas-liquid interface	*P^* (MPa)*	*22.28*
Gas constant	*R (J/mol·K)*	*8.314*
Molar volume (water film)	*V_m (m^3/mol)*	*18×10^{-6}*

4.4.2 Model Validation

Jin (2014) used a Monte Carlo model (MC) to conduct molecular simulations on methane and moisture adsorptions inside 4-nm clay pores. The findings showed that when methane and water are simultaneously adsorbed in clay pores, a clay surface is occupied by a water film; methane gets adsorbed on this moisture film. The average methane density ($\bar{\rho}_{CH_4}$) inside 4-nm slit pores (H = 4nm) under various water saturations is given below (Jin, 2014).

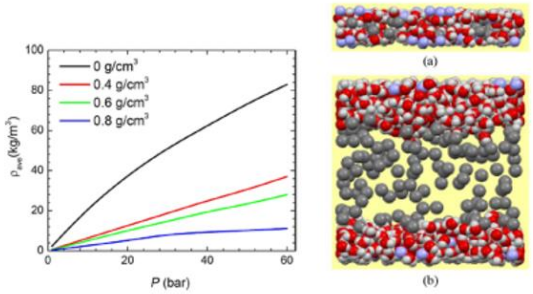

Figure 4-8 Methane average density and water-gas distribution in clay pores (Jin, 2014)

The average methane density in pores is (Jin, 2014):

$$\bar{\rho}_{CH_4} = \frac{(n_{ad-silt} + n_{bulk-silt}) \cdot M_{CH_4}}{A_{slit} \cdot H} \tag{4.17}$$

where M_{CH_4} refers to the mole mass of methane, which is 16 g/mol.

There exists a certain distance from the solid surface to methane molecules, the effective interlayer spacing of a slit pore is:

$$H^* = H - 2\Delta \tag{4.18}$$

where Δ is the distance from the oxygen atoms in water molecules to the oxygen atoms in the clay and, which is around 0.27 - 0.315 nm. In our calculations, Δ = 0.3 nm. After considering this distance, the molar amount of free gas in the pores is:

$$n^*_{bulk-silt} = n_{bulk-silt} \cdot \frac{H - 2\Delta}{H} \tag{4.19}$$

Combining equations (4.3), (4.19) and (4.21) when there is no water in the pores (ρ_{H2O} = 0 g/cm^3), the average methane density can be expressed as:

$$\overline{\rho}_{CH_4} = \frac{n_{T-slit} \cdot M_{CH_4}}{A_{slit} \cdot H} = (\frac{2K}{H} \cdot \frac{P}{P + P_L} + \frac{H - 2\Delta}{H} \cdot \frac{P}{ZRT}) \cdot M_{CH_4} \tag{4.20}$$

Combining equations (4-8), (4-18) and (4-20), when the pores contain moisture (ρ_{H2O} = 400 g/cm^3 or 600 g/cm^3), the average methane density will be described as:

$$\overline{\rho}_{CH_4} = \frac{n_{T-silt} \cdot M_{CH_4}}{A_{slit} \cdot H} = (\frac{2\Gamma^*}{H} \cdot \frac{P}{P + P^*} + \frac{H - 2(\Delta + h)}{H} \cdot \frac{P}{ZRT}) \cdot M_{CH_4} \tag{4.21}$$

where the thickness of the liquid film is:

$$h = \frac{\overline{\rho}_{H_2O}}{\rho^*_{H_2O}} \cdot \frac{H}{2} \tag{4.22}$$

where ρ^*_{H2O} represents the liquid water density, whose value is 1 g/cm^3; M_{CH4} refers to the mole mass of methane, whose value is 16 g/mol.

We apply Peng-Robinson model to the compression factor calculation for free gas (Peng and Robinson, 1976). Under various temperature conditions, the calculation results of the compression factor *Z* are shown in Figure 4-9.

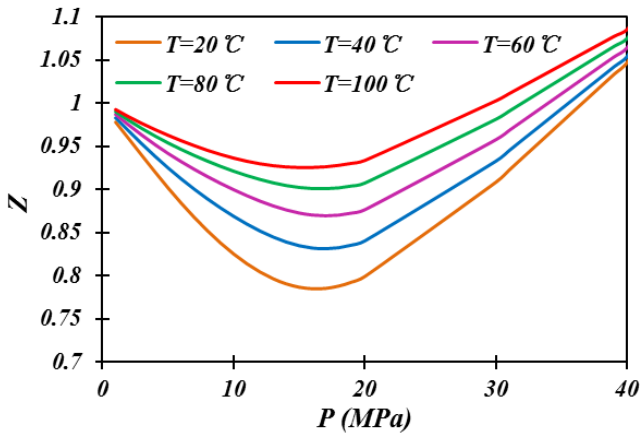

Figure 4-9 Compressibility factors (Peng and Ronbinson, 1976)

At a temperature of 298K, using the data in equations (22), equation (23), and Table 4-2, we apply our proposed model to the calculation of the average methane density ($\overline{\rho}_{CH_4}$) in pores with various water saturations. We have then matched our calculated results with Jin's simulated data, and as given by Figure (4-10), the good match has proven the reliability of our proposed model.

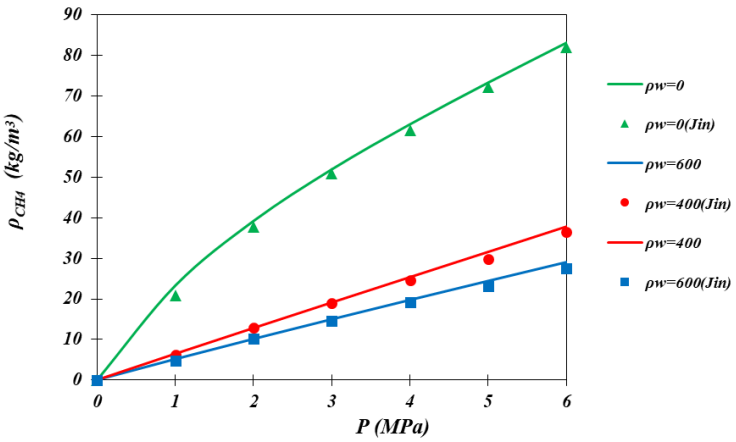

Figure 4-10 Results comparisons (ρ_{CH4})

Furthermore, the adsorption amount at the gas-liquid interface in Jin's molecular simulations ($\Gamma_{ad\text{-}slit}(sim)$) can be derived from the $\overline{\rho}_{CH_4}$ value:

$$\Gamma_{ad-slit}(sim) = \frac{n_{T-silt} - n^{*}_{bulk-silt}}{2A_{slit}} = \frac{1}{2} \cdot \left(\frac{\overline{\rho}_{CH_4} \cdot H}{M_{CH_4}} - \frac{P \cdot (H - 2\Delta - 2h)}{ZRT} \right) \tag{4.23}$$

The derived $\Gamma_{ad\text{-}slit}(sim)$ values through equation (4.26) are then compared to the $\Gamma_{ad\text{-}slit}(sim)$ values derived from our model, shown to be consistent with each other (Figure 4-11). The adsorption capacity linearly increases as the pressure rises within a low pressure range; then the amount of adsorbed methane tends to remain stable as the pressure continues to increase

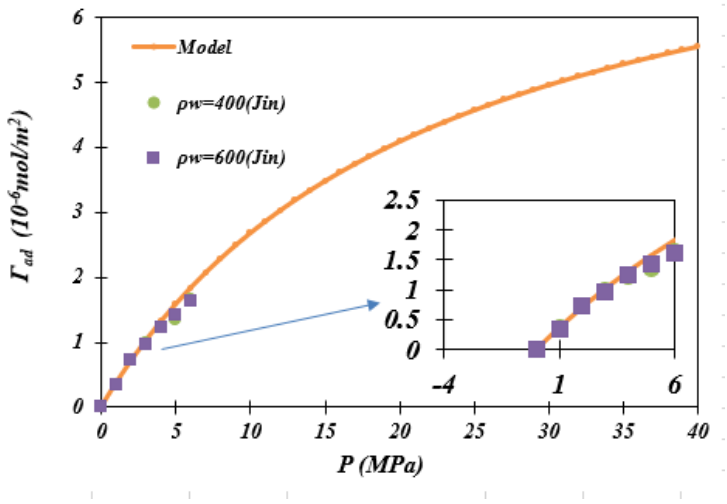

Figure 4-11 Results comparisons (Γ_{ad})

4.4.3 Model Application

The validation results have shown that our proposed adsorption model has a high degree of reliability. Therefore, based on our model, the amount of methane adsorbed on a clay pore surface can be quantitatively evaluated under different water saturations in actual conditions.

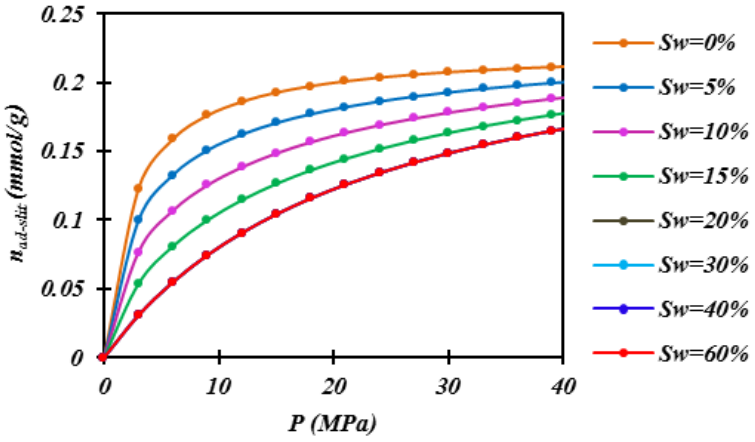

Figure 4-12 Methane adsorption isotherms under different water saturations in slit pores

According to equations (4-15) and (4-17), the isothermal adsorption curves of slit pores and capillaries within a pressure range of 0 - 40MPa and a water saturation range of 0 - 60% at a temperature of 298K are calculated, which are given by Figure 4-12 and Figure 4-13.

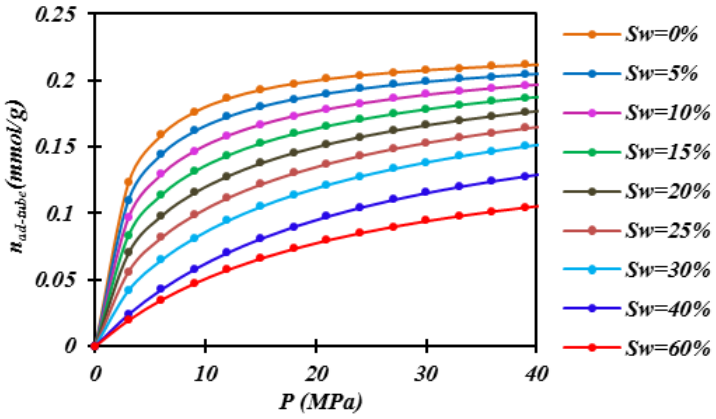

Figure 4-13 Methane adsorption isotherms under different water saturations in capillaries

In addition, we have also analyzed how the ratio of the natural gas adsorption capacity of wet clay to the natural gas adsorption capacity of dry clay ($n_{ad\text{-}wet}$/ $n_{ad\text{-}dry}$) changes with an increasing water saturation under a pressure of 10 MPa (Figure 4-14). Seen from Figure 4-14, in slit pores, the methane adsorption capacity declines as water saturation rises. When S_w reaches 20%, the surface of the pore is with monolayer moisture coverage. At this point, the amount of adsorbed methane has decreased by 55.4%. When S_w >20, the water content is not affecting the natural gas adsorption capacity over a longer timeframe (in Figure 4-12, the isothermal adsorption curves coincide when S_w = 20%, 30%, 40% and 60%). And when they are saturated with water (S_w = 100%), the slit pores lose their adsorption capacity. For capillaries, the impact of the rising moisture content is not linear, and an inflection point occurs when S_w = 36%. Before water saturation reaches 36%, the pore surface is only partially covered by water, so the adsorption process of methane on the clay surface is a competitive adsorption with water. After the water saturation gets higher than 36%, the major cause of the down-going trend in the gas adsorption capability is that water has gradually occupied the pore space, bringing about a lessening of the effective surface area, which is a situation that is not reflected in the slit pore model. With a high moisture content (S_w = 80%), the methane adsorption capacity will be reduced by about 80%, as

the methane adsorption capacity in capillaries is more sensitive to moisture content compared with that in slit pores.

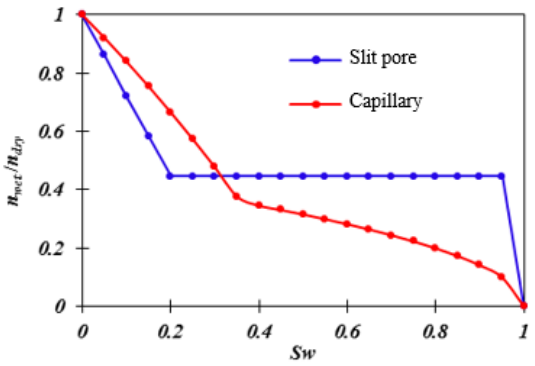

Figure 4-14 Relationship between adsorption capacity and water saturation

4.5 Impact of Temperature

Our study only uses T=298 K as an example for analysis, but the temperature system in actual shale reservoirs is complicated and methane adsorption capacity in shale is largely dependent on temperature.

(1) Gas-clay Interface Adsorption

The adsorbed methane amount on the dry clay surface decreases significantly with a rising temperature. The maximum capacity per unit area (K) hardly changes with temperature. Temperature mainly changes the Langmuir pressure (P_L), which characterizes the methane-clay interaction force. A larger P_L value corresponds to a weaker gas-solid interaction and leads to a lower methane adsorption capacity. As temperature increases, the gas-solid interaction gets weaker. So the P_L value increases with a rising temperature. When the temperature changes from 35. 4 ℃ to 65. 4 ℃, the P_L value of montmorillonite increases from 2. 22 MPa to 3. 93 MPa; P_L value of illite increases from 4. 73 MPa to 6. 75 MPa; P_L value of kaolinite increases from 5. 58 MPa to 9. 52 MPa (Ji et al., 2012). In our study, temperature is fixed (T=298 K; P_L =2.5 MPa). Based on

adsorption thermodynamics, it is derived by Xia and Tang (2012) that the Langmuir constant ($1/P_L$) of the gas-solid interface is related to temperature (T) as:

$$\ln(1/P_L) = \frac{q_{st}}{RT} + c \tag{4.27}$$

where q_{st} is the adsorption heat, kJ/mol; c is constant.

According to equation (4.27), the P_L values at various temperatures can be obtained to draw the isotherm adsorption curves on the surface of dry clay.

(2) Gas-water Interface Adsorption

As presented by the Gibbs equation, the gas-water surface tension gradient and the natural gas adsorption capacity are closely connected. With surface tension being extremely sensitive to temperature, temperature largely influences the gas adsorption capacity at the methane-water interface. Experimental data (Jennings and Newman, 1971) have shown how the methane-water surface tension changes with gas pressure at various temperatures, as shown in Figure 4-4. We have used equation (4.7) to fit the relationship between pressure and surface tension; and we have found that the value of Γ* does not change with temperature while the value of P* (Langmuir pressure for the gas-liquid interface) is 22.28, 50.13, 120.22 MPa, at a temperature of 23.3℃, 100. 0℃, 176.6 ℃, respectively. A higher temperature leads to a higher P^* value and thus results in a lower methane adsorption capacity at the methane-water interface. Using the fitting parameters for the methane-water surface tension in Table 4-1, combined with equation (4.8), the methane adsorption amount on the water film surface at a temperature of 23.3℃, 100. 0℃, 176.6 ℃ can be calculated (Figure 4-15).

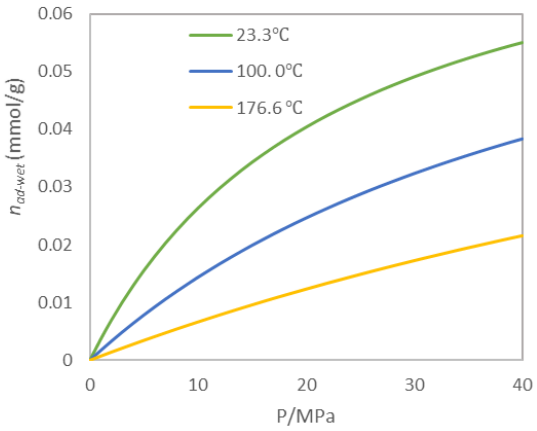

Figure 4-15 Methane adsorption curves with different temperatures (gas-liquid interface interaction)

However, current researches on gas-water surface tension under different temperature and pressure conditions mainly use semi-empirical equations combined with experimental data; and there is no reasonable theoretical model. Therefore, to quantify the impact of temperature on our model for the gas-liquid adsorption still needs further study.

4.6 Summary

(i) Under dry conditions, methane adsorption on the clay surface belongs to a gas-solid interaction, and the Langmuir isothermal adsorption equation can be utilized for the calculation of the adsorption amount. When the surface of clay is completely covered by moisture, with methane adsorbed on the thin liquid film, methane adsorption is a gas-liquid interaction, for which the Gibbs adsorption equation can be leveraged.

(ii) Combining the Langmuir equation and Gibbs equation, we have established a mathematical model to calculate the methane adsorption amount in shale clay pores (slit pores and capillary) at different water saturations, in which the water coverage coefficient is introduced. Molecular simulation data in 4 nm pores (Jin, 2014) have been used to validate our proposed model,

and are shown to be consistent with our calculated results, confirming the reliability of our mathematical model.

(iii) The isothermal adsorption curves in slit pores and capillaries with various moisture contents at a temperature of 298K are calculated, and the influence of moisture is analyzed. In summary, the adsorption capacity for methane generally declines with an increasing moisture content. Compared with slit pores, the gas adsorption capability of capillaries is more sensitive to moisture content because the existence of water reduces the effective methane adsorption area of capillaries.

Chapter 5 Water Distribution and Methane Adsorption Characteristics in Porous Media

5.1 Pore Distribution

There are three types of clay mineral pores based on their different structures, as shown in Figure 5-1: inter-granular pores formed by the compaction and deposition of mineral particles, inter-crystalline pores formed during the process of mineral diagenesis, and, finally, an interlayer space formed by the distance between crystal layers inside the clay crystal.

Generally, the size of intergranular pores in clay is more than 100 nm, and there are various types such as planar slit pores, triangular pores, multi-layer cave pores, and scattered circular pores (Zolfaghari and Dehghanpour, 2015). The inter-crystalline pores inside clay particles are generally within 100 nm, while the interlayer space of clay minerals is usually 1 to 2 nm, or even a mere 0.7mm.

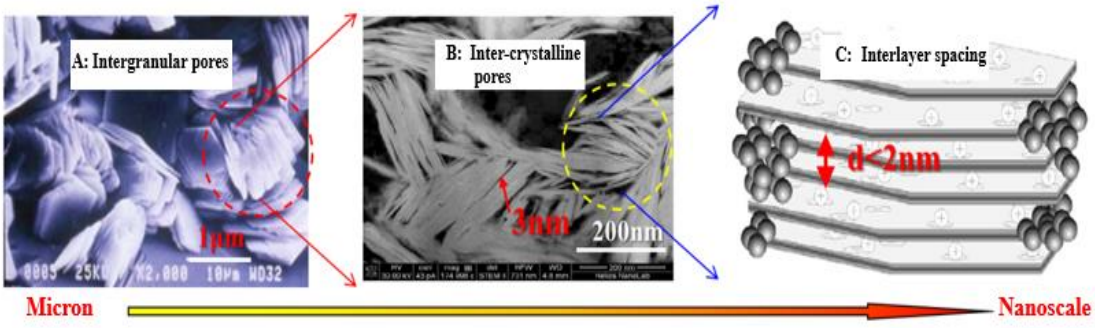

Figure 5-1 Clay minerals pores

Given the complicated pore distribution of actual clay minerals, to make the subsequent calculations easier, we will assume that a pore size distribution in porous media conforms to a log-normal distribution function (Figure 5-2):

$$\phi_i(x) = \frac{1}{x\sqrt{2\pi}\sigma}\exp[-\frac{1}{2}(\frac{\ln x - u}{\sigma})^2] \tag{5.1}$$

where ϕ_i is the pore volume fraction; σ is the standard deviation, whose value is 0.5; u is the logarithmic mean, which is 1.65.

The average pore diameter can be determined as:

$$H^*(D^*) = \exp(u - \sigma^2) \tag{5.2}$$

$$\phi_i = \frac{V_i}{V_T} \tag{5.3}$$

When σ=0.5, u=1.65; we can get the average pore diameter: $H^*(D^*)$ = 4.01nm.

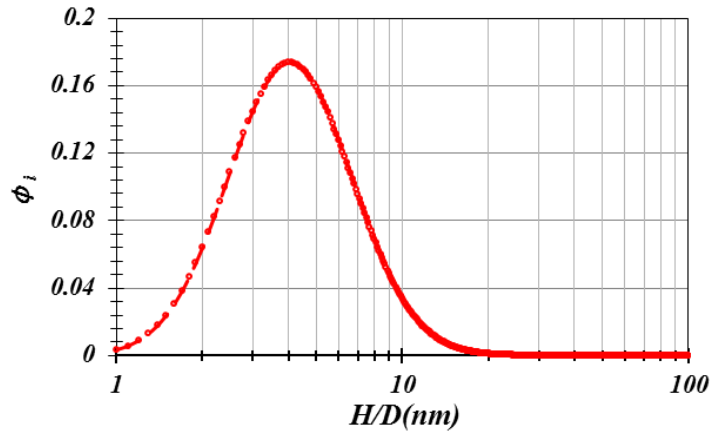

Figure 5-2 Pore distribution characteristics

5.2 Water Distribution in Porous Media

As has been shown, shale reservoirs generally hold two kinds of bound water: (i) capillary moisture in small pores blocking the pore space (ii) a liquid film adsorbed on the pore surface when the pores are large. From Chapter 3, we know that under the same relative humidity, water saturations in pores of varying sizes are also different. For either slit pore or capillary, under the same relative humidity, smaller nanopores always correspond to higher water saturations.

In this section, we will use thermodynamic principles and adsorption theory to quantify the water distribution characteristics in: (i) porous media formed by various sizes of slit pores (slit-pore porous media) and (ii) porous media formed by various sizes of capillaries (capillary porous media). Our other assumptions remain the same as in Chapters 3 and 4.

5.2.1 Slit Pore Model

For a single slit pore, the water film thickness and water saturation are quantified as follows (see Chapter 3 for further details):

$$\begin{aligned}
&\Pi_{slit}(h) = \Pi_1(h) + \Pi_2(h) + \Pi_3(h) \\
&\Pi_1(h) = \frac{A_H}{h^3} + \frac{\varepsilon\varepsilon_0}{8\pi}\frac{(\zeta_1 - \xi_2)^2}{h^2} + ke^{-\frac{h}{\lambda}} \\
&\Pi_2(h) = \frac{A_H}{(H-h)^3} + \frac{\varepsilon\varepsilon_0}{8\pi}\frac{(\zeta_1 - \xi_2)^2}{(H-h)^2} + ke^{-\frac{H-h}{\lambda}} \\
&\Pi_3(h) = \frac{A_H}{(H-2h)^3}
\end{aligned} \tag{5.4}$$

$$\Pi_{slit}(h) = -\frac{RT}{V_m}\ln\frac{P_v}{P_0} \tag{5.5}$$

$$S_{w-slit}(i) = \frac{2h}{H} \tag{5.6}$$

For porous media consisting of different sized slit pores, the total water volume (including a water film and capillary water) is the sum of the water volume inside single pores of different sizes, which is given as:

$$V_{wT} = \sum_{i=1}^{i=n} h_i \cdot A_i = \sum_{i=1}^{i=n} 2 \cdot h_i \cdot \frac{V_i}{H_i} = \sum_{i=1}^{i=n} S_{wi} \cdot V_i \tag{5.7}$$

Therefore, the total water saturation can be expressed as:

$$S_{w-slit} = \frac{V_{wT}}{V_T} = \sum_{i=1}^{i=n} S_{w-slit}(i) \cdot \frac{V_i}{V_T} = \sum_{i=1}^{i=n} S_{w-slit}(i) \cdot \phi_i \tag{5.8}$$

Using equations (5.4)-(5.8), the total water saturations under various relative humidity for slit-pore porous media with a certain pore distribution are calculated (Figure 5-3). The water saturation rises with the rising relative humidity. Before the relative humidity reaches 0.8, the water saturation increases slowly. After that, the water saturation rises more sharply.

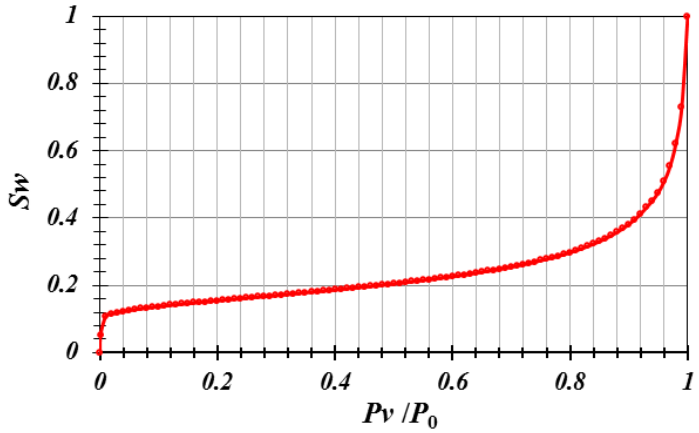

Figure 5-3 Relationship between water saturation and natural gas humidity in slit-pore porous media

Since the water saturation is a monotonic function of relative humidity, the relative humidity can be derived from the total water saturation. The gas phase is assumed to be a continuous phase at a unified system with the same pressure, temperature and humidity. Therefore, with a given total water saturation in the porous media, we can obtain the humidity, and then calculate the pore water saturations. The water saturations of various sizes of slit pores with different relative humidity conditions can be obtained (Figure 5-4). When the water saturation in the reservoir is 10%, 21%, 43%, and 62%, the corresponding relative humidity of natural gas in the reservoir is 0.01, 0.56, 0.93, and 0.98, respectively.

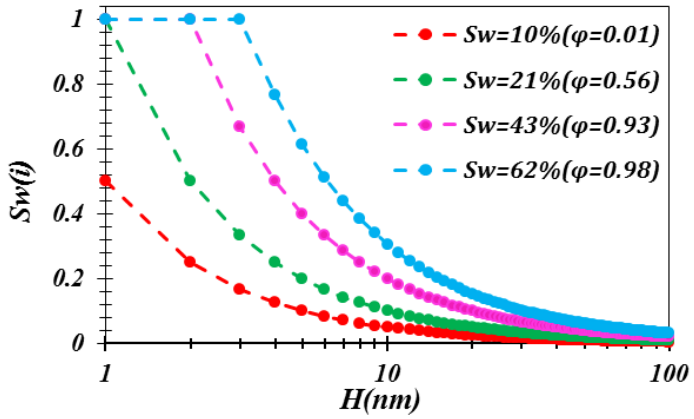

Figure 5-4 Water saturation distribution characteristics of various sizes of slit pores

In the case of low water saturation (S_w=10%), all pores possess a water film (S_{wi}<1), indicating that none of the pores are blocked by capillary moisture. As the moisture content of the reservoir increases, however, small pores are gradually filled by capillary water (S_{wi}=1), while the large pores adsorb their water films (S_{wi}<1). When the water saturation of the porous media reaches 21%, the 1-nm pores are blocked by moisture; with the water saturations being 43% and 62%, 2-nm and 3-nm pores will also be filled with water. The molecular simulation results (Jin Z, 2014) showed: when pores are filled with water molecules, methane molecules cannot enter the pores (because clay is strongly hydrophilic). Therefore, tiny pores that are filled by capillary moisture will lose their adsorption capacity for methane.

5.2.2 Capillary Model

In a single capillary, the water film thickness can be expressed as follows (see Chapter 3 for the derivation details):

$$\prod_{capillary}(h)=\frac{r}{r-h}\prod_{flat}(h)+P_c=\frac{r}{r-h}\prod_{flat}(h)+\frac{\gamma}{r-h} \tag{5.9}$$

$$\Pi_{capillary}(h) = -\frac{RT}{V_m}\ln\frac{P_v}{P_0} \tag{5.10}$$

$$S_{w-capillary}(i) = 1-(1-\frac{h}{r})^2 \tag{5.11}$$

For porous media, the total water saturation can be expressed as:

$$S_{w-capillary} = \frac{V_w}{V_T} = \sum_{i=1}^{i=n} S_{w-capillary}(i)\cdot\frac{V_i}{V_T} = \sum_{i=1}^{i=n} S_{w-capillary}(i)\cdot\phi_i \tag{5.12}$$

Using equations (5.9)–(5.12), the total water saturations can be obtained under the log-normal pore distribution (Figure 5-3). Before the relative humidity reaches 0.4, the water saturation increases slowly with the increasing relative humidity. After that, the water saturation rises more rapidly.

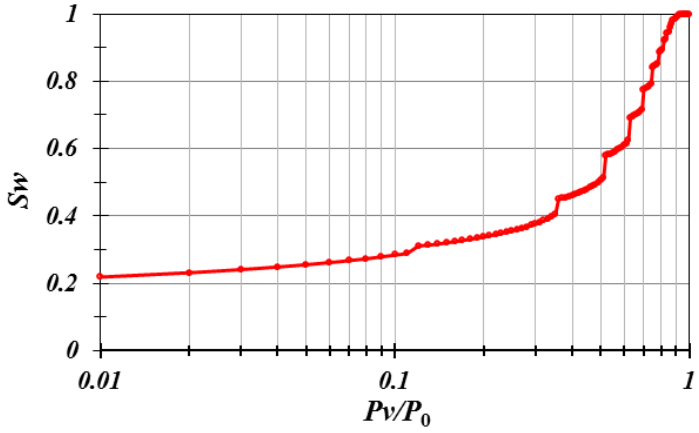

Figure 5-5 Water saturation vs. natural gas humidity in capillary porous media

Similarly, the water saturation distribution in different sized capillaries under different relative humidity are obtained (Figure 5-6). Compared with slit pores, the capillary has a stronger ability to adsorb water. Even under extremely low relative humidity (*RH*=0.01), 1nm capillaries are completely filled by capillary moisture. As relative humidity increases, the water saturation of

the reservoir increases, and more small pores are blocked by moisture. With total water saturation being 30%, 45%, 58%, 69%, and 78%, the capillaries with diameters of 2nm, 3nm, 4nm, 5nm and 6nm will gradually be blocked, and the corresponding relative humidity will be 0.12, 0.36, 0.52, 0.63 and 0.70, respectively. Under high relative humidity conditions (*RH*=0.98), the capillaries within 100 nm will get blocked by capillary moisture. However, in slit pores, when the relative humidity is 0.98, only the pores within 3nm will be filled with moisture.

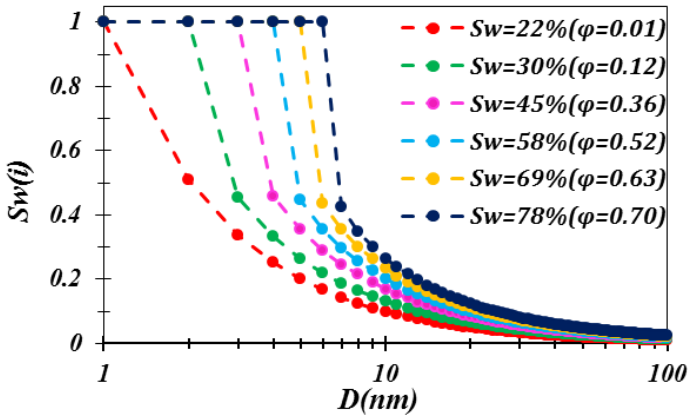

Figure 5-6 Water saturation distribution characteristics of different sized capillaries under different relative humidity

5.3 Methane Adsorption in Porous Media

5.3.1 Slit Pore Model

In Chapter 4, the methane adsorption isotherms of a single slit pore with different water saturations were obtained. We now extend our findings to the case of porous media in this section. Through the derivation in Chapter 4, the adsorption capacity for methane in slit pores under various water saturations can be expressed as:

$$\begin{cases} n_{ad-dry} = 2 \cdot A_{slit} \cdot K \cdot \dfrac{P}{P + P_L}; \quad S_w = 0 \\ n_{ad-mix} = (1-\alpha) \cdot n_{ad-dry} + \alpha \cdot n_{ad-wet}; \quad 0 \le S_w \le S_{mon} \\ n_{ad-wet} = 2 \cdot A_{slit} \cdot \Gamma^* \cdot \dfrac{P}{P + P^*}; \quad S_{mon} \le S_w \le 1 \end{cases} \tag{5.13}$$

where S_{mon} is the water saturation with a single layer of water molecules covering the pore wall, %;

$$S_{mon} = \frac{2 \times 0.4}{H_i} \tag{5.14}$$

and α is the water coverage coefficient. For a single pore, it is expressed as:

$$\alpha_i = S_{wi} / S_{mon} \tag{5.15}$$

In theory, the maximum value of α is 1. Therefore, when α>1, α=1. The methane adsorption amount in a single slit pore can be expressed as:

$$n_{ad}(i) = [(1-\alpha_i) \cdot K \cdot \frac{P}{P + P_L} + \alpha_i \cdot \Gamma^* \cdot \frac{P}{P + P^*}] \cdot A_i \tag{5.16}$$

The total gas adsorption amount should be described as:

$$n_{ad-T} = \sum_{i=1}^{i=n} n_{ad-i} = \sum_{i=1}^{i=n} [(1-\alpha_i) \cdot K \cdot \frac{P}{P + P_L} + \alpha_i \cdot \Gamma^* \cdot \frac{P}{P + P^*}] \cdot A_i \tag{5.17}$$

where α_i is the water coverage coefficient, %; $n_{ad\text{-}i}$ is the natural gas adsorption capacity inside a single pore, mmol/g.

Based on equation (5.17) and equation (5.8), the total methane adsorption capacity of the slit-pore porous media can be obtained when the total water saturation is $S_{w\text{-}T}$. In this process, if a

different relative humidity (P_v/P_0) is given first, the gas adsorption capability of slit-pore porous media under different water saturations can be calculated.

Using the log-normal pore distribution in Figure 5-2 and the basic data in Table 5-1, we can calculate the gas adsorption amount in a slit-pore porous media under different water saturations. Results are given by Figure 5-7.

Table 5-1 Basic parameters for methane adsorption model in slit-pore porous media

Parameter	***Symbol (unit)***	***Value***
Temperature	*T(K)*	*298*
Pressure	*P(MPa)*	*0~40*
Maximum adsorption capacity per unit area (gas-solid)	$K(mmol/m^2)$	*0.0075*
Langmuir pressure of the gas-solid interface	$P_L(MPa)$	*2.5*
Maximum adsorption capacity per unit area (gas-liquid)	$\Gamma^*(mmol/m^2)$	*0.00864*
Langmuir pressure of the gas-liquid interface	*P*(MPa)*	*22.28*
Gas constant	*R(J/mol·K)*	*8.314*
Hamaker constant	A_H *(J)*	1×10^{-20}
Mole volume (water film)	$V_m(m^3/mol)$	18×10^{-6}
Pore volume	$V_T(cm^2/g)$	*0.023*
Specific surface area	$A(m^2/g)$	*10*

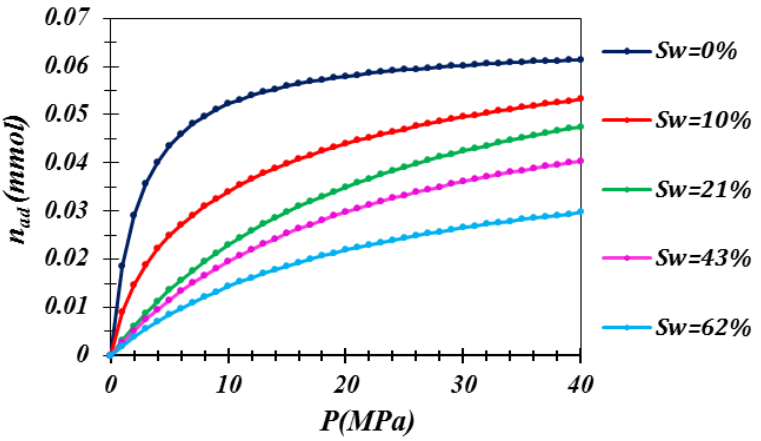

Figure 5-7 Methane adsorption isotherms of slit-pore porous media under different water saturations

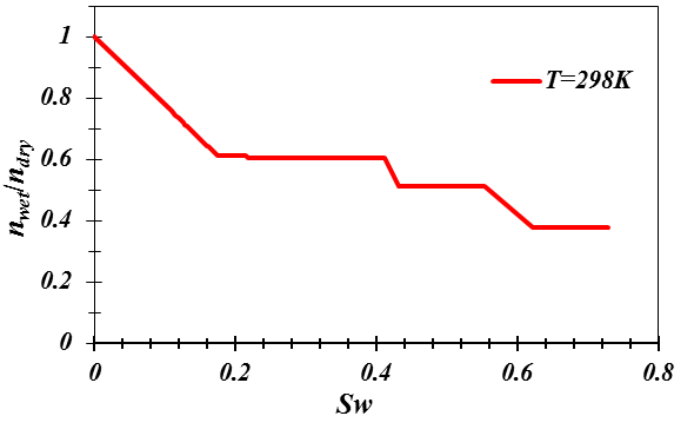

Figure 5-8 Gas adsorption capacities in slit-pore porous media under various water conditions

Meanwhile, the ratio of $n_{\text{ad-wet}}/n_{\text{ad-dry}}$ under various water conditions at 20 MPa is shown in Figure 5-8. The downward trend and the different inflection points in Figure 5-8 can be explained as follows:

(i) Before the thickness of the adsorbed thin wetting film reaches 0.4 nm and as the water saturation increases, the methane adsorption mechanism gradually transitions from gas-solid adsorption to gas-liquid adsorption, resulting in a linear decline of methane adsorption capacity alongside a rise in water saturation (0.4 nm is the thickness of monolayer water molecules). The inflection point of S_w=16% corresponds to the 0.4-nm average thickness of the wetting film, with

the pore surface covered with exactly monolayer of moisture. Thus, the adsorption characteristics of methane have completely changed from gas-solid to gas-liquid adsorption.

(ii) After the thickness of the adsorbed liquid film reaches 0.4 nm, methane is only adsorbed on the wetting film. If no pores are blocked by moisture, the adsorbed amount will remain constant as the water saturation changes. However, as the total water saturation continues to increase, some small pores will be completely filled with capillary moisture and lose their methane adsorption capacity, causing the total amount of adsorbed methane to decline. This explains the three inflection points when S_w=21%, 43% and 62% in Figure 5-8. From the water saturation distribution characteristics of slit-pore porous media (Figure 5-4), we already know that: when the total water saturation arrives at 21%, the 1-nm pores are choked by moisture; with water saturation being above 43% and 62%, the 2-nm and 3-nm pores will also be completely filled with water. This exactly corresponds to the three inflection points in Figure 5-8.

5.3.2 Capillary Model

From Chapter 4, we know that the methane adsorption amount in the capillary under different water saturations can be expressed as:

$$\begin{cases} n_{ad-dry} = K \cdot A_{capillary} \cdot \dfrac{P}{P+P_L}; \quad S_w = 0 \\ n_{ad-mix} = (1-\alpha) \cdot n_{ad-dry} + \alpha \cdot n_{ad-wet}; \quad S_w = \alpha S_{mon} (0 \le \alpha \le 1) \\ n_{ad-wet} = A_{capillary} \cdot \sqrt{1-Sw} \cdot \Gamma^* \cdot \dfrac{P}{P+P^*}; \quad S_{mon} \le S_w \le 1 \end{cases} \tag{5.18}$$

where S_{mon} is the water saturation with the capillary wall surface covered by exactly one layer of adsorbed water molecules, %;

$$S_{mon} = \frac{(D_i / 2)^2 - (D_i / 2 - 0.4)^2}{(D_i / 2)^2} \tag{5.19}$$

and α is the water coverage coefficient. For a single capillary, it can be expressed as:

$$\alpha_i = S_{wi} / S_{mon} \tag{5.20}$$

In theory, the maximum value of α is 1. Therefore, when α>1, α=1. The methane adsorption amount in a single capillary can be expressed as:

$$n_{ad}(i) = [(1-\alpha_i) \cdot K \cdot \frac{P}{P+P_L} + \alpha_i \cdot \sqrt{1-S_{wi}} \cdot \Gamma^* \cdot \frac{P}{P+P^*}] \cdot A_i \tag{5.21}$$

The total adsorbed natural gas is:

$$n_{ad-T} = \sum_{i=1}^{i=n} n_{ad-i} = \sum_{i=1}^{i=n} [(1-\alpha_i) \cdot K \cdot \frac{P}{P+P_L} + \alpha_i \cdot \sqrt{1-S_{wi}} \cdot \Gamma^* \cdot \frac{P}{P+P^*}] \cdot A_i \tag{5.22}$$

where $\alpha(i)$ is the water coverage coefficient, %; $n_{ad\,(i)}$ refers to the adsorption capacity of a capillary, mmol/g.

From equations (5.22) and (5.12), the total gas adsorption capacity of the capillary porous media can be obtained when the total water saturation is $S_{w\text{-}T}$. In this process, if a different relative humidity (Pv/P_0) is given first, we are able to calculate the gas adsorption capacity under various moisture conditions, shown in Figure 5-9.

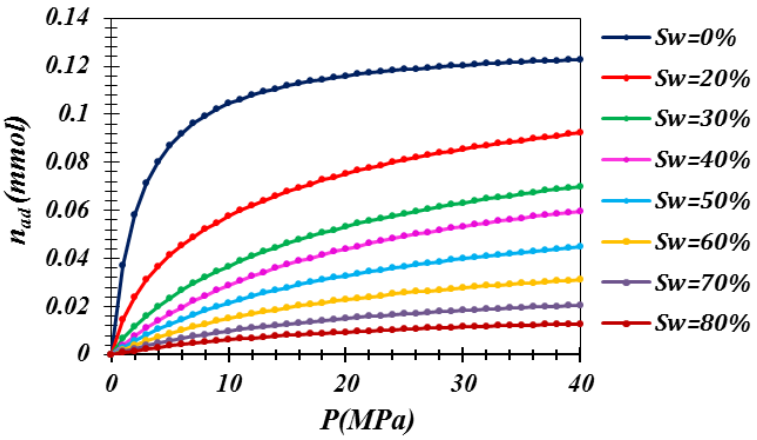

Figure 5-9 Gas adsorption isotherms in capillary porous media under various water saturations

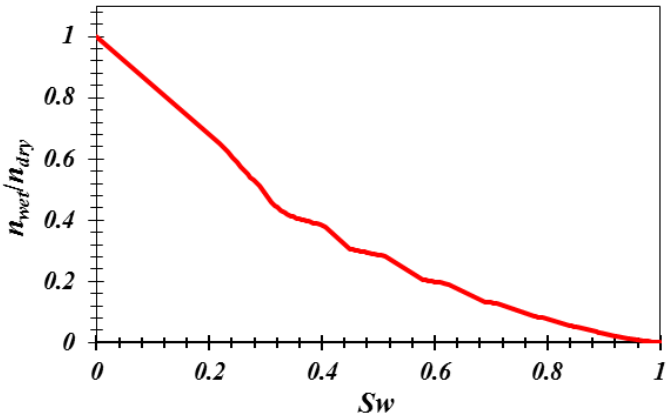

Figure 5-10 Methane adsorption capacity vs. water saturation in capillary porous media under the pressure of 20MPa

Meanwhile, the methane adsorption capacity ($n_{ad\text{-}wet}/n_{ad\text{-}dr}$) vs. water saturation ($S_w$) curve under 20 MPa is shown in Figure 5-10. Compared with the slit pore case, the porous media characterized by capillaries are more sensitive to moisture. Indeed, the change of methane adsorption capacity alongside water saturation in capillaries is unlike the slit pore case with its multiple inflection points Instead, there is a more continuous downward trend. This is because after the water film thickness reaches 4 nm (e.g., meaning that the capillary surface with monolayer

moisture coverage and methane adsorption is completely a gas-liquid interaction), two major mechanisms can explain the deduction in the adsorption capability of the capillary porous shale: (i), the effective adsorption area of a single capillary decreases as the water saturation increases; and (ii), some capillaries are completely filled with water as the water saturation increases. These two reasons dominate the methane adsorption capacity of the capillary porous media while methane adsorption capacity in slit pore porous media is only dominated by reason (ii). When the water saturation is greater than 20%, small fluctuations are seen in the methane adsorption capacity ($n_{ad\text{-}wet}/n_{ad\text{-}dr}$) vs. water saturation ($S_w$) curve in Figure 5-10, and are explained by reason (ii).

The distribution characteristics of water saturation in the different sized capillaries of capillary porous media (Figure 5-6) show that: when water saturation of the reservoir reaches 30%, 45%, 58%, 69% and 78%, the 2nm, 3nm, 4nm, 5nm and 6nm, pores will gradually be filled with water. This corresponds to the small fluctuations in Figure 5-10 when S_w=30%, 45%, 58%, 69% and 78%.

5.4 Summary

(i) We have calculated the total water saturations under different relative humidity conditions in a porous shale with a log-normal distribution (PSD). The water saturation is found to go up as humidity goes up. In a slit pore case, the water saturation goes up slowly with a humidity rise before humidity reaches 0.8, after which point the water saturation rises more sharply with a rising *RH*. Yet in a capillary case, before the relative humidity reaches 0.4, water saturation increases slowly as relative humidity increases. After that, water saturation rises sharply.

(ii) The water saturations in different sized slit pores and capillaries have been calculated so the moisture distributions in different sized nanopores have also been obtained. As the water saturation in porous media (S_w) increases, some small pores get filled with moisture (S_{wi}=1). For

slit pore cases, with the reservoir's water saturation being 21%, 43% and 62% (corresponding relative humidity is 0.01, 0.56, 0.93, and 0.98), the 1-nm, 2-nm and 3-nm pores get completely filled with water. For capillary cases, with the water saturation being 30%, 45%, 58%, 69%, and 78% (corresponding relative humidity is 0.12, 0.36, 0.52, 0.63 and 0.70), the 2-nm, 3-nm, 4-nm, 5-nm and 6-nm capillaries are subsequently filled with water.

(iii) Methane adsorption isotherms of the porous media under different water saturations have been calculated and methane adsorption capacities with various moisture contents under the pressure of 20 MPa have also been obtained. In slit pore cases, as the water saturation increases, there're two major mechanisms for the deduction in gas adsorption capability: ① the conversion from gas-solid to gas-liquid adsorption; ② small pores completely filled by water losing their methane adsorption capacity (S_w=21%, 43% and 62%). In capillary cases, as the water saturation increases, there are two reasons to account for the decline in gas adsorption capability:① the deduction in the effective adsorption area of a single capillary;② the decrease in the effective adsorption area of porous media because some small capillaries are completely filled with water (S_w=30%, 45%, 58%, 69% and 78%).

Chapter 6 Conclusions and Recommendations

In this thesis, mathematical models to calculate gas adsorption capacity and water film thickness in both single nanoscale shale clay pores and the shale clay porous media have been established and validated, in the slit pore case and capillary case. Through a series of calculation results by our proposed models, we have analyzed the water distribution features and their influence in gas adsorption capability in shale clay pores. The effect of pore shape on water saturation and methane adsorption features have also been discussed.

6.1 Conclusions

(1) Under the ultra-low water saturation, the adsorption-evaporation thermodynamic equilibrium between liquid moisture and gaseous water inside shale clay micro-pores has been analyzed and shown to be the main factor for controlling the moisture content in a reservoir. By considering disjoining pressure and microscopic forces, we have constructed a mathematical model to calculate the thickness of the thin aqueous film. Taking the pore shape into consideration, the established model is divided into a slit pore case and a capillary case.

(2) Using our proposed model, the water saturation and aqueous film thickness, inside a single slit pore and inside a single capillary, under different relative humidity, are calculated. Also, the capillary condensation phenomenon in small nanopores is observed. That is, when the relative humidity is less than 1, the pores will be filled by capillary water. In a 5-nm slit pore, capillary condensation is observed when the relative humidity turns to 0.75; while in a 5-nm capillary, the critical value of relative humidity for capillary condensation is 0.39. Based on our calculation results, the pore-wall potential is mainly influenced by a pore size and pore shape. For either slit pores or capillary, the capillary condensation phenomenon in smaller pores is more significant. For pores with the same pore size (slit width or capillary diameter), capillaries have thicker

aqueous films and higher water saturations than slit pores, and thus condensation is more likely to occur in capillaries. For example, when the relative humidity is 0.6, the water saturation in a 5-nm slit pore is 21% while the water saturation in a 5 nm-capillary is 47%.

(3) Under dry conditions, natural gas adsorption in shale clay pores is a gas-solid interaction, and the adsorption amount can be derived utilizing the Langmuir adsorption equation. When a clay surface is completely covered by water, methane adsorption belongs to a gas-liquid interaction and can be calculated by the Gibbs adsorption equation.

(4) Combining Langmuir equation for a gas-solid interaction and the Gibbs equation for a gas-liquid interaction, we have established a mathematical model to calculate the methane adsorption amount in shale clay pores at different water saturations, in which the water coverage coefficient is introduced. Molecular simulation data in 4 nm pores has been used to validate our proposed model, which are consistent with our calculation results, indicating that our proposed model is reliable.

(5) The isothermal adsorption curves in a single slit pore and a single capillary within the water saturation range of 0 - 60% and pressure of 0 - 40 MPa at a temperature of 298K are calculated. Through our calculation results, we find that methane adsorption capacity generally declines with a rising moisture content. Through our calculation, with the water saturation in a 4-nm slit pore being 20%, methane adsorption capacity is decreased by 55.4%, compared with dry conditions; when the water saturation in a 4-nm capillary is 36%, methane adsorption capacity is decreased by 80%. Compared with a slit pore, methane adsorption capacity in a capillary is more sensitive to moisture content because the existence of water causes a reduction in the effective methane adsorption area in the capillary.

(6) We have calculated the total water saturations in porous shale following a log-normal pore size distribution (PSD). Water saturation in porous media increases with an increase in relative humidity. In a slit pore case, before the relative humidity reaches 0.8, water saturation increases slowly with an increase in relative humidity. When humidity gets higher than 0.8, water saturation rises shrply. This is similar to the capillary case, but the critical value of relative humidity is 0.4 rather than 0.8.

(7) The water saturations in different sized slit pores and capillaries under different relative humidity conditions have also been calculated so the water saturation distribution characteristics inside different sized pores have been obtained. As the water saturation in porous media (S_w) increases, some tiny pores will gradually be filled with capillary moisture (S_{wi}=1). For example, when the water saturation of the slit-pore porous media reaches 21%, 43% and 62%, the 1-nm, 2-nm and 3-nm slit pores are completely filled with moisture; with the water saturation of the capillary porous shale being 30%, 45%, 58%, 69% and 78%, the 2-nm, 3-nm, 4-nm, 5-nm and 6-nm capillaries are subsequently filled with water.

(8) Methane adsorption isotherms of the porous media under different water saturations have been calculated and the gas adsorption capacities with various moisture contents under the pressure of 20 MPa have also been obtained. In slit pore cases, as the water saturation increases, two major mechanisms lead to the decline in gas adsorption capability: (i) the conversion of gas adsorption features from gas-solid to gas-liquid; (ii) small pores completely filled by water losing their gas adsorption capability. With the water saturation of the slit-pore porous media being 43%, the methane adsorption capacity is deceased by 50% compared with dry conditions. In capillary cases, as the water saturation increases, two main reasons result in the decline in gas adsorption ability: (i) the deduction in the effective adsorption area of a single capillary; (ii) the deduction in

the effective adsorption area of the whole reservoir because some small capillaries are completely filled with water. When the water saturation of the capillary porous media reaches 45%, the methane adsorption capacity is deceased by 70% compared with dry conditions.

6.2 Future recommendations

(1) Only molecular simulation results in 4-nm pores (Jin, 2014) have been used to validate our proposed model. In future studies, we can conduct experiments for water saturation distributions and gas adsorption capacities inside differently sized shale nanopores to further validate the proposed model.

(2) In our model we have only considered the water content in inorganic pores of shale. Although the water content in kerogen pores is relatively low in the gas generation stage, there is still some water adsorbed near the functional groups. We can expect a model which integrates both organic and inorganic pores in the future.

(3) To extend our proposed model form a single pore case to porous media, we have assumed a pore size distribution (PSD) to follow a log-normal function. The pore size distributions of actual shale clay samples can be utilized in our model in future studies.

(4) Our study only uses T=298 K as an example for analysis, but the temperature system in actual shale reservoirs is complicated and methane adsorption capacity in shale is largely dependent on temperature. We have discussed the impact of temperature on our calculations and our future recommendations for introducing temperature into current proposed model in Chapter 4.

References

Bennion, D. B., Thomas, F. B., & Ma, T. (2000, January). Formation damage processes reducing productivity of low permeability gas reservoirs. In SPE Rocky Mountain Regional/Low-Permeability Reservoirs Symposium and Exhibition. Society of Petroleum Engineers.

Bennion, D. B., & Thomas, F. B. (2005). Formation damage issues impacting the productivity of low permeability, low initial water saturation gas producing formations.

Chalmers, G. R., & Bustin, M. R. (2010). PS the effects and distribution of moisture in gas shale reservoir systems.

Chen, S., Han, Y., Fu, C., Zhu, Y., & Zuo, Z. (2016). Micro and nano-size pores of clay minerals in shale reservoirs: Implication for the accumulation of shale gas. Sedimentary geology, 342, 180-190.

Churaev, N. V. (1995). Contact angles and surface forces. Advances in colloid and interface science, 58(2-3), 87-118.

Churaev, N. V. (1995). The relation between colloid stability and wetting. Journal of colloid and interface science, 172(2), 479-484.

Churaev, N. V., Starke, G., & Adolphs, J. (2000). Isotherms of capillary condensation influenced by formation of adsorption films: 1. calculation for model cylindrical and slit pores. Journal of colloid and interface science, 221(2), 246-253.

Costanza, M. S., & Brusseau, M. L. (2000). Contaminant vapor adsorption at the gas− water interface in soils. Environmental science & technology, 34(1), 1-11.

Costanza, M. S., & Brusseau, M. L. (2000). Contaminant vapor adsorption at the gas− water interface in soils. Environmental science & technology, 34(1), 1-11.

Curtis, M. E., Ambrose, R. J., Sondergeld, C. H., & Rai, C. S. (2011, January). Transmission and scanning electron microscopy investigation of pore connectivity of gas shales on the nanoscale. In *North American unconventional gas conference and exhibition*. Society of Petroleum Engineers.

Derjaguin, B. V., Churaev, N. V., Muller, V. M., & Kisin, V. I. (1987). Surface forces. New York: Consultants Bureau.

Gasparik, M., Ghanizadeh, A., Bertier, P., Gensterblum, Y., Bouw, S., & Krooss, B. M. (2012). High-pressure methane sorption isotherms of black shales from the Netherlands. Energy & fuels, 26(8), 4995-5004.

Gosiewska, A., Drelich, J., Laskowski, J. S., & Pawlik, M. (2002). Mineral matter distribution on coal surface and its effect on coal wettability. Journal of Colloid and Interface Science, 247(1), 107-116.

Grant, R. J., & Manes, M. (1966). Adsorption of binary hydrocarbon gas mixtures on activated carbon. Industrial & Engineering Chemistry Fundamentals, 5(4), 490-498.

Gu, Y., Ding, W., Yin, S., Yin, M., & Xiao, Z. (2018). Adsorption characteristics of clay minerals in shale. Petroleum Science and Technology, 36(2), 108-114.

Ho, C. K., & Webb, S. W. (Eds.). (2006). Gas transport in porous media (Vol. 20). Springer Science & Business Media.

Hongjun, W. A. N. G., Feng, M. A., Xiaoguang, T. O. N. G., Zuodong, L., Zhang, X., Zhenzhen, W. U., & Liuyan, Y. A. N. G. (2016). Assessment of global unconventional oil and gas resources. *Petroleum Exploration and Development*, *43*(6), 925-940.

Hu, Y., Devegowda, D., Striolo, A., Phan, A., Ho, T. A., Civan, F., & Sigal, R. F. (2014). Microscopic dynamics of water and hydrocarbon in shale-kerogen pores of potentially mixed wettability. Spe Journal, 20(01), 112-124.

Hu, Y., Devegowda, D., Striolo, A., Phan, A., Ho, T. A., Civan, F., & Sigal, R. (2015). The dynamics of hydraulic fracture water confined in nano-pores in shale reservoirs. Journal of Unconventional Oil and Gas Resources, 9, 31-39.

Hu, Y., Devegowda, D., & Sigal, R. (2016). A microscopic characterization of wettability in shale kerogen with varying maturity levels. Journal of Natural Gas Science and Engineering, 33, 1078-1086.

Jahediesfanjani, H., & Civan, F. (2007). Determination of multi-component gas and water equilibrium and non-equilibrium sorption isotherms in carbonaceous solids from early-time measurements. Fuel, 86(10-11), 1601-1613.

Jennings Jr, H. Y., & Newman, G. H. (1971). The effect of temperature and pressure on the interfacial tension of water against methane-normal decane mixtures. Society of Petroleum Engineers Journal, 11(02), 171-175.

Ji, L., Zhang, T., Milliken, K. L., Qu, J., & Zhang, X. (2012). Experimental investigation of main controls to methane adsorption in clay-rich rocks. Applied Geochemistry, 27(12), 2533-2545.

Jin, Z., & Firoozabadi, A. (2013). Methane and carbon dioxide adsorption in clay-like slit pores by Monte Carlo simulations. Fluid Phase Equilibria, 360, 456-465.

Jin, Z., & Firoozabadi, A. (2014). Effect of water on methane and carbon dioxide sorption in clay minerals by Monte Carlo simulations. Fluid Phase Equilibria, 382, 10-20.

Koga, Y. (2017). Chapter II - Solution Thermodynamics—Use of the Second and Third Derivatives of G. In Y. Koga (Ed.), Solution Thermodynamics and its Application to Aqueous Solutions (Second Edition) (pp. 27-61): Elsevier.

Kondo, S., Ishikawa, T., & Abe, I. (2006). Translated by Li G X. Adsorption Science, Chemical Industry Press, Beijing, 140.

Korb, J. P., Nicot, B., Louis-Joseph, A., Bubici, S., & Ferrante, G. (2014). Dynamics and wettability of oil and water in oil shales. The Journal of Physical Chemistry C, 118(40), 23212-23218.

Langmuir, I. (1917). The evaporation, condensation and reflection of molecules and the mechanism of adsorption. Journal of the Franklin Institute, 183(1), 101-102.

Li, F., Wang, M., Liu, S., & Hao, Y. (2019). Pore characteristics and influencing factors of different types of shales. Marine and Petroleum Geology, 102, 391-401.

Luo, P., Zhong, N., Khan, I., Wang, X., Wang, H., Luo, Q., & Guo, Z. (2019). Effects of pore structure and wettability on methane adsorption capacity of mud rock: Insights from mixture of organic matter and clay minerals. Fuel, 251, 551-561.

Merkel, A., Fink, R., & Littke, R. (2016). High pressure methane sorption characteristics of lacustrine shales from the Midland Valley Basin, Scotland. Fuel, 182, 361-372.

Newsham, K. E., Rushing, J. A., & Lasswell, P. M. (2003, January). Use of vapor desorption data to characterize high capillary pressures in a basin-centered gas accumulation with ultra-low connate water saturations. In SPE Annual Technical Conference and Exhibition. Society of Petroleum Engineers.

Newsham, K. E., Rushing, J. A., Lasswell, P. M., Cox, J. C., & Blasingame, T. A. (2004, January). A comparative study of laboratory techniques for measuring capillary pressures in tight gas sands. In SPE Annual Technical Conference and Exhibition. Society of Petroleum Engineers.

Ong, S. K., & Lion, L. W. (1991). Mechanisms for trichloroethylene vapor sorption onto soil minerals. Journal of environmental quality, 20(1), 180-188.

Passey, Q. R., Bohacs, K., Esch, W. L., Klimentidis, R., & Sinha, S. (2010, January). From oil-prone source rock to gas-producing shale reservoir-geologic and petrophysical characterization of

unconventional shale gas reservoirs. In International oil and gas conference and exhibition in China. Society of Petroleum Engineers.

Peng, D. Y., & Robinson, D. B. (1976). A new two-constant equation of state. Industrial & Engineering Chemistry Fundamentals, 15(1), 59-64.

Rezaee, R. (Ed.). (2015). Fundamentals of gas shale reservoirs. John Wiley & Sons.

Ross, D. J., & Bustin, R. M. (2008). Characterizing the shale gas resource potential of Devonian–Mississippian strata in the Western Canada sedimentary basin: Application of an integrated formation evaluation. AAPG bulletin, 92(1), 87-125.

Ross, D. J., & Bustin, R. M. (2009). The importance of shale composition and pore structure upon gas storage potential of shale gas reservoirs. Marine and petroleum Geology, 26(6), 916-927.

Sang, G., Liu, S., & Elsworth, D. (2019). Water vapor sorption properties of Illinois shales under dynamic water vapor conditions: Experimentation and modeling. Water Resources Research, 55(8), 7212-7228.

Starov, V. M., Velarde, M. G., & Radke, C. J. (2007). Wetting and Spreading Dynamics. CRC Press.

Sui, H., Zhang, F., Wang, Z., Wang, D., & Wang, Y. (2020). Effect of kerogen maturity, water content for carbon dioxide, methane, and their mixtures adsorption and diffusion in kerogen: A computational investigation. Langmuir.

Takahashi, S., & Kovscek, A. R. (2010). Wettability estimation of low-permeability, siliceous shale using surface forces. Journal of Petroleum Science and Engineering, 75(1-2), 33-43.

Tang, X., Zhang, T., Zhang, J., Sun, X., Wu, C., & Jin, Z. (2020). Effects of pore fluids on methane sorption in the Lower Bakken Shales, Williston Basin, USA. Fuel, 282, 118457.

Tissot, B. P. (1984). Recent advances in petroleum geochemistry applied to hydrocarbon exploration. AAPG bulletin, 68(5), 545-563.

Ungerer, P. (1990). State of the art of research in kinetic modelling of oil formation and expulsion. Organic Geochemistry, 16(1-3), 1-25.

U.S., Energy Information Administration, World Shale Resource Assessments, https://www.eia.gov/analysis/studies/worldshalegas.

U.S. Energy Information Administration, U.S. Crude Oil and Natural Gas Proved Reserves, Year-end 2018, https://www.eia.gov/naturalgas/crudeoilreserves.

Van Oss, C. J., & Giese, R. F. (1995). The hydrophilicity and hydrophobicity of clay minerals. Clays and Clay minerals, 43(4), 474-477.

Xia, X., & Tang, Y. (2012). Isotope fractionation of methane during natural gas flow with coupled diffusion and adsorption/desorption. Geochimica et Cosmochimica Acta, 77, 489-503.

Yang, R., Jia, A., He, S., Hu, Q., Dong, T., Hou, Y., & Yan, J. (2020). Water adsorption characteristics of organic-rich Wufeng and Longmaxi Shales, Sichuan Basin (China). Journal of Petroleum Science and Engineering, 107387.

Zhiltsov, S. S., & Zonn, I. S. (2016). The evaluation of the world potential of shale gas reserves. In Shale Gas: Ecology, Politics, Economy (pp. 17-24). Springer, Cham.

Zhou, W., Lu, Y., Gao, C., Li, W., Zhang, Y., Li, X., & Dong, J. (2013). Effects of Flow Pattern and Pore Size on Immiscible Continuous Three-Phase Displacement. Energy & fuels, 27(2), 717-724.

Zou, J., Rezaee, R., Xie, Q., & You, L. (2019). Characterization of the combined effect of high temperature and moisture on methane adsorption in shale gas reservoirs. Journal of Petroleum Science and Engineering, 182, 106353.